Analysis of radiative transfer in a turbulent sooting jet flame using a Monte Carlo method coupled to large eddy simulation

Pedro Rodrigues, Olivier Gicquel, Benedetta Franzelli, Nasser Darabiha, Ronan Vicquelin

To cite this version:

Pedro Rodrigues, Olivier Gicquel, Benedetta Franzelli, Nasser Darabiha, Ronan Vicquelin. Analysis of radiative transfer in a turbulent sooting jet flame using a Monte Carlo method coupled to large eddy simulation. Journal of Quantitative Spectroscopy and Radiative Transfer, 2019, 235, pp.187-203. 10.1016/j.jqsrt.2019.07.003 . hal-02196698

HAL Id: hal-02196698
https://hal.science/hal-02196698v1

Submitted on 29 Jul 2019

HAL is a multi-disciplinary open access archive for the deposit and dissemination of scientific research documents, whether they are published or not. The documents may come from teaching and research institutions in France or abroad, or from public or private research centers.

L'archive ouverte pluridisciplinaire **HAL**, est destinée au dépôt et à la diffusion de documents scientifiques de niveau recherche, publiés ou non, émanant des établissements d'enseignement et de recherche français ou étrangers, des laboratoires publics ou privés.

Analysis of radiative transfer in a turbulent sooting jet flame using a Monte Carlo method coupled to large eddy simulation

Pedro Rodrigues[a], Olivier Gicquel[a], Benedetta Franzelli[a], Nasser Darabiha[a], Ronan Vicquelin[a]

[a]*Laboratoire EM2C, CNRS, CentraleSupélec, Université Paris-Saclay,*
8-10 rue Joliot Curie, 91192 Gif-sur-Yvette cedex, France

Abstract

Due to the relevant contribution of radiative transfer in the global energy balance of many industrial combustion systems, a deep understanding and accurate modelling of gas and soot radiative transfer is necessary. This topic is addressed here numerically in a canonical turbulent sooting configuration, i.e. an ethylene-air jet diffusion flame. The study is based on a coupled Monte Carlo - Large Eddy Simulation. In order to introduce as much physical details as possible, a recently-developed sectional model is used for soot particles description and the radiative transfer equation is solved using a Monte-Carlo method. A cK model describes gas radiative properties and the Rayleigh's theory is considered for soot particles properties. Numerical results are compared to experimental data on radiative intensity measured along the flame height to validate the proposed methodology. Then, the different radiative contributions i.e. emission-absorption, gas-soot, are analyzed to study the nature of the radiative heat transfer in the investigated flame. Finally, turbulence-radiation interactions are quantified for the total mean emitted, absorbed and radiative powers. Closure of these effects on the mean emitted power is proposed and discussed. Opposite effects of turbulence-radiation interactions are observed for

---

*Corresponding author:
Email address: ronan.vicquelin@centralesupelec.fr (Ronan Vicquelin)

Preprint submitted to Journal of Quantitative Spectroscopy & Radiative Transfer July 29, 2019

the gaseous and the soot contributions: the increase in mean emitted power for the gaseous phase is due to temperature fluctuations whereas a decrease of the solid phase contribution appears from a negative temperature-soot volume fraction correlation.

Keywords:
Thermal Radiation, Soot, Sectional model, Monte Carlo method, Large Eddy Simulation, Turbulence Radiation Interaction

---

1. Introduction

In industrial burners and combustion chambers, heat exchanges are of multiple types: conduction, convection and radiation. In some industrial applications, radiative heat transfer can be significant and must therefore be quantified and controlled to, preserve the combustor materials on the one hand, and to efficiently maximize the heat exchange in several applications, on the other hand. Several contributions to thermal radiation are distinguished. Thermal radiation from gaseous species, in particular burst gases, constitutes the non-luminous contribution. In the presence of soot particles, radiative heat transfer can be greatly enhanced with an additional luminous contribution. Numerical modeling is therefore necessary for the design of practical combustion systems in order to understand and predict such heat exchanges.

The modeling of gaseous combustion products evolution along with their thermal radiation has been largely studied in the literature and more and more predictive simulations have been achieved by accounting for accurate gas radiative properties and the necessary modeling of turbulence radiation interactions (TRI) in RANS simulations [1, 2, 3, 4]. These efforts have been pursued with coupled 3-D large-eddy simulations (LES) [5, 6, 7] that benefit from a better description of turbulent and reactive flows and a resolution of most turbulence-radiation interactions in such unsteady computations. Taking into account the additional contribution of soot particles in the radiative heat transfer of turbulent flames, which are generally encountered in industrial applications, requires the modeling of these particles evolution and of the complex coupling that exists between soot, turbulence, flame and thermal radiation.

To do so, Tesse *et al.* [8] proposed a RANS modeling of a turbulent jet sooting diffusion flame coupled with a Monte Carlo radiation solver. For soot particles description, an empirical model to estimate the soot volume fraction evolution was used. Wang *et al.* [9] have also proposed coupled radiation RANS simulations based on an empirical model for soot particles evolution. In their study, the resolution of the radiative transfer equation (RTE) is based on the spherical harmonics method. Pal *et al.* [10] have compared coupled RANS modeling of a turbulent jet sooting diffusion flame with spherical harmonics method, DOM method and Monte Carlo methods in terms of accuracy and cost. Again, an empirical model for soot particles was used in order to retrieve a good agreement with experimental measurements. Mehta *et al.* [11]s have also considered a coupling approach between RANS for turbulence description and Monte Carlo resolution of the RTE. For the description of soot particles, a detailed validated soot model based on a method of moments was retained. More recently, Consalvi and Nmira [12, 13] have investigated turbulent sooting jet diffusion flames based on RANS calculations, finite volume method for the RTE resolution and a semi-empirical model for soot particles predictions.

Contrary to RANS modeling, large-eddy simulations enable not only the main resolution of turbulence-radiation interactions at the LES mesh scale mentioned previously but also the description of complex soot-turbulence interactions. Recent studies have then considered such coupled large-eddy simulations of sooting flames with thermal radiation. Gupta *et al.* [6] have proposed such an approach for the investigation of luminous flames coupled with a Monte Carlo method for the resolution of the RTE. However, the used empirical model for the soot volume fraction, provided as a function of the local equivalence ratio, lacks of physics and generality. Lecocq *et al.* [14] have also investigated soot radiation in coupled LES simulations based on a DOM solver of the RTE and a semi-empirical model for soot predictions.

In the present study, a large-eddy simulation of a turbulent diffusion jet flame is carried out with an advanced modeling of the solid phase based on a sectional representation of the particles size distribution (PSD). The radiative transfer equation is solved using a Monte-Carlo solver [15] based on the emission-reciprocity method (ERM) [16]. Detailed gas radiative properties are considered based on a narrow-band cK model. Finally, the soot radiative properties are described by the Rayleigh's theory. To our knowledge, such a simulation represents the first example of a large-eddy simulation based on a soot sectional model coupled with a radiative transfer solver. Soot modeling accounts for a detailed description of the chemical and the collisional processes governing soot production and has already been validated on laminar [17] and turbulent [18] flames. In addition, choosing the Monte Carlo solver for the RTE resolution yields accuracy to the computation of the associated radiative transfer. Even if uncertainties remain in the soot formation model and in the particles radiative properties, the simulation achieves a step forward towards accurate description of interactions between soot, turbulence and radiation with state-of-the-art models and numerical approaches.

Beyond the demonstration of feasibility, the numerical results are first validated against experiments to assess the accuracy of such a coupled simulation. Then, the analysis of the captured physical phenomena in LES fields allows for a detailed study of radiative heat transfer in the considered jet flame. The role of soot particles in thermal radiation is identified and quantified from a macroscopic to local and spectral points of view. Radiative interactions between gaseous and solid phases are evaluated along with the role of radiative absorption. Finally, the effects of TRI captured by the coupled LES on average fields of radiative powers are studied while validating a model for the mean radiative emission.

The contents of the study are presented as follows: Section 2 presents the considered experimental configuration and details the numerical models. The numerical results and their validation are then shown in Sec. 3. For this, temperature and soot volume fraction profiles are first compared with the experimental profiles together with the radiative intensity. To highlight the need for coupled simulations to account for both absorbed and emitted radiations, the obtained fields of gaseous and solid quantities are compared to two uncoupled simulations. The first one assumes no radiative heat losses. The second simulation accounts for radiation through a simple optically thin model [18]. Finally, in Sec. 4 the radiative heat transfer in both gaseous and solid phases obtained with the coupled simulation is analyzed, followed by a quantification of turbulence-radiation interaction effects on the mean emitted, absorbed and total radiative power fields.

2. Studied configuration and numerical models

2.1. Experimental configuration

The configuration chosen for the simulation is a turbulent non-premixed flame fed with pure ethylene that has been characterized experimentally at Sandia [19]. This configuration corresponds to a turbulent jet with Reynolds number $\mathrm{Re}_D = 20\,000$, based on the fuel injector of the main jet $D = 3.2$ mm. The corresponding bulk velocity is $v_{\mathrm{fuel}} = 54.7$ m/s. Temperature and $X_{\mathrm{O}_2}/X_{\mathrm{N}_2}$ measurements [20] are available along with LII soot volume fraction measurements [19] and spatially resolved measurements of radiant emission [19], which correspond to directive measurements of the radiative intensity averaged over a small solid angle $\Omega_1 = 1.065 \times 10^{-4}$ sr at a radial distance of 500 mm from the flame axis.

The main jet tube presents an outer diameter of 4.6 mm and is surrounded by another tube with an inner diameter of 15.2 mm, and an outer diameter of 19.1 mm. Pilot flames are located between both tubes for the stabilization of the flame. Their total heat release corresponds to only 2% of the heat release of the main jet. Finally, a coflow of air at $v_{\mathrm{air}} = 0.6$ m/s surrounds the whole injection system. The inlet temperatures of all the flows, except the pilot, are equal to 294 K. For the pilot flame, a flame temperature equal to 2 296 K has been estimated from an adiabatic calculation with an equivalence ratio of $\Phi = 0.9$.

2.2. Numerical model

2.2.1. LES modeling of gaseous and solid phases

The numerical and the modeling approaches used for the description of the gaseous and solid phases in the present coupled simulation are identical to the setup used in a previous uncoupled simulation of the same flame [18]. They are here briefly summarized.

A tabulated method is used here to describe the gaseous phase chemistry. This method is based on the FPV (Flamelet Progress Variable) [21] model where any thermochemical variable ψ is obtained from a look-up table. To construct this table, the stationary laminar diffusion flame equations are solved and parametrized as a function of both mixture fraction Z and a normalized progress variable. The impact of heat losses is taken into account by considering non-adiabatic flames (RFPV model [22]) and adding an enthalpy defect parameter Θ to the parameterization. Then, in order to include in the table the effects of the subgrid interactions between chemistry and turbulence on the gaseous phase, a presumed probability density (PDF) function approach is considered [22]: a beta-PDF parametrized by the segregation factor of the mixture fraction S_Z is used to describe the mixture fraction distribution Z, while a δ-Dirac is used for the statistical distributions of the progress variable C and the heat loss parameter Θ. Thus, each filtered thermochemical variable $\widetilde{\psi}$ is pre-tabulated and can be retrieved using a 4-D RFPV table: $\widetilde{\psi} = \widetilde{\mathcal{R}}(\widetilde{Z}, S_Z, C, \Theta)$. In the LES simulation, four transport equations for the mixture fraction $\widetilde{Z}$, the mixture fraction variance Z_v, the non-normalized progress variable $\widetilde{Y_C}$ and the enthalpy $\widetilde{h}$ are added to the Navier-Stokes equations to determine the four parameters of the table and extract from the table the needed information.

In the present simulation, the KM2 kinetic mechanism [23], developed specifically for the prediction of soot precursors, has been used to describe the gaseous phase chemistry and then to construct the table. The table contains 100 points in each $\widetilde{Z}$ and C dimensions and 20 points in each S_Z and Θ dimensions.

Being strongly characterized by unsteadiness effects, information for precursors and soot particles cannot be extracted from the table and need to be transported. Therefore, for the description of the soot precursors evolution, a relaxation model [24] is used whereas for the solid phase a sectional model, already validated in laminar [17] and turbulent [18] configurations, is considered here. Such an approach allows a discretized representation of the soot particles size distribution in the particles volume space. Formation of soot particles from the different mechanisms, i.e. nucleation, condensation, surface growth, oxidation and coagulation, can then be described in details by accounting for the size of soot particules. While this approach is often deemed expansive for computational fluid dynamics, its recent combination with LES has demonstrated its feasibility, validation and adequacy to describe detailed informations about soot particles population and their dynamic [18]. In this approach, small soot particles are considered as spherical particles with a volume v and a diameter d for $v < v_{\mathrm{lim}} = \pi d_{\mathrm{lim}}^3/6$ with $d_{\mathrm{lim}} \approx 10$ nm. For soot particles presenting a volume $v > v_{\mathrm{lim}}$, they are considered as aggregates of primary particles with the same primary particle diameter $d_p = d_{\mathrm{lim}}$. In the case where the soot particle is considered as spherical, the primary particle diameter d_p is equal to the particle diameter d. This description of soot morphology impacts directly the description of condensation, surface growth, oxidation and coagulation phenomena. The interactions between turbulence and the chemical and physical dynamics of soot production are taken into account by adapting a subgrid model for the hybrid method of moments [25] to the sectional technique, as explained in [18]. A total of 28 equations are therefore transported in order to describe the soot particles size distribution dynamics.

2.3. Radiation model

2.3.1. Radiative properties

For gaseous species, only the radiative properties of CO_2 and H_2O species are considered. The contribution of other species in conventional flames being at least one order of magnitude lower than those of these two species [26]. The radiative properties are modeled through a narrow-band approach: the cK model [27] based on updated parameters from Riviere and Soufiani [26]. These parameters have been generated for applications at atmospheric pressure in the 300-4000K temperature range. They are based on the CDSD-4000 database for CO_2 absorption spectra [28] and HITEMP 2010 H_2O absorption spectra [29]. For H_2O, 44 spectral bands, with widths varying from 50 cm^{-1} to 400 cm^{-1}, are considered between 150 cm^{-1} and 9200 cm^{-1}. CO_2 absorbs radiation in only 17 of these bands. The cK database is made of 7-point Gauss quadrature per band for each gaseous component, leading to 1022 pseudo-spectral points, since 49 quadrature points are used in the 17 overlapping bands.

For the radiation of soot particles, 93 spectral bands (44 of them are common to the gas) have been introduced between 150 and 29 000 cm^{-1}. This enables to capture the correct effect of soot absorption coefficient for a temperature range between 300 K and 2500 K. Using the RDG/RDG-FA theory for radiative properties of soot aggregates, the soot absorption coefficient κ_ν^{soot} of an ensemble of soot particles is equivalent to the one obtained from Rayleigh's theory [30]:

$$\kappa_\nu^{\text{soot}} = C_0 f_V \nu \tag{1}$$

where ν is the wavenumber (in m^{-1}), f_V is the soot volume fraction and C_0 is given by:

$$C_0 = \frac{36\pi n k}{(n^2 - k^2 + 2)^2 + 4n^2k^2}, \tag{2}$$

with $m = n - ik$ corresponding to the complex index of refraction of soot particles, taken equal to $m = 1.57 - 0.56i$ [31].

Concerning the total extinction, scattering by soot particles is neglected. This is justified by the fact that in our simulation the maximum primary particle diameter d_p is around 10 nm, which corresponds to a size parameter $\overline{x_p} = 2\pi d_p \nu$ lower than 0.1 for all the considered wavenumbers. Scattering is then small compared to absorption according to RDG theory for the considered index of refraction so that it can be neglected. While the retained soot sectional approach allows to describe some features of the soot morphology such as its impact on condensation, surface growth, oxidation and coagulation phenomena, the associated effects on soot radiative properties are neglected in this manuscript since soot radiation is calculated only from total information on f_v. Further developments are needed to be incorporated in future studies.

2.3.2. Monte Carlo resolution of the Radiative Transfer Equation

The reciprocal formalism is used here in order to solve the radiative transfer equation. The radiation computational domain in discretized into N_v and N_f isothermal finite cells of volume V_i and faces of area S_i respectively. The exchanged power between two nodes i and j is given by:

$$P_{ij}^{\text{exch}} = \int_{\nu=0}^{+\infty} \kappa_\nu(T_i) \left[I_\nu^\circ(T_j) - I_\nu^\circ(T_i)\right] \int_{4\pi} A_{ij\nu} d\Omega d\nu \tag{3}$$

where $I_\nu^\circ(T_i)$ is the blackbody spectral emissive intensity at temperature T_i. $A_{ij\nu}$ accounts for all the paths between emission from the node i and absorption in any point j, after transmission, scattering and possible wall reflections along the paths. The total radiative power of a node i is computed as $P_i^R = \sum_j P_{ij}^{\text{exch}}$ with a Monte Carlo method. The Emission-based Reciprocity Method (ERM) [16] is used here in order to compute the radiative power of each node. For calculation of the radiative intensities at the measurement probe locations, as they are placed in cold regions, the Optimized Emission-based Reciprocity Method (OERM) [32] is used in order to converge efficiently the Monte-Carlo simulation in such regions. To allow the comparison with experiments, the mean radiative intensity I_q^{R} at a probe location q is directly linked to the directive radiative flux $\Phi_q^{\Omega_1}$ of a domain face q over the solid angle Ω_1 through:

$$I_q^{\text{R}} = \frac{1}{\Omega_1} \Phi_q^{\Omega_1} = \frac{1}{\Omega_1} \int_{\nu=0}^{\infty} \int_{\Omega_1} I'_\nu(\mathbf{u}, \mathbf{r})\, \mathbf{u} \cdot \mathbf{n} \, \mathrm{d}\Omega \, d\nu, \tag{4}$$

where $I'_\nu(\mathbf{u}, \mathbf{r})$ is the local intensity at the position $\mathbf{r}$ travelling in the direction $\mathbf{u}$, and $\mathbf{n}$ is the unity vector normal to the probe detector. Following OERM,

$\Phi_q^{\Omega_1}$ is evaluated as:

$$\begin{aligned}\Phi_q^{\Omega_1} &= \sum_{j=1}^{N_f+N_v} \Phi_{qj}^{\Omega_1,\mathrm{exch}} \\ &= \sum_{j=1}^{N_f+N_v} \left[\left(1 - \left(1 - \frac{\Omega_1}{2\pi}\right)^2\right) \sigma T_{\max}^4 \int_{\nu=0}^{\infty} \frac{I_\nu^\circ(T_q)}{I_\nu^\circ(T_{\max})} \right. \\ &\left. \left[\frac{I_\nu^\circ(T_j)}{I_\nu^\circ(T_q)} - 1\right] \int_{\Omega_1} A_{ij\nu} f_{\Omega_q}^{\mathrm{wall}}(\Omega) f_{\nu_q}(\nu, T_{\max}) d\Omega d\nu \right]\end{aligned} \tag{5}$$

with the wavenumber and direction distributions

$$\begin{aligned} f_{\nu_q}(\nu, T_{\max}) &= \frac{I_\nu^\circ(T_{\max})}{\int_{\nu=0}^{\infty} I_\nu^\circ(T_{\max}) d\nu}, \\ f_{\Omega_q}^{\mathrm{wall}}(\Omega) d\Omega &= f_{\theta_q}^{\mathrm{wall}}(\theta) d\theta f_{\psi_q}^{\mathrm{wall}}(\psi) d\psi, \end{aligned} \tag{6}$$

and

$$\begin{aligned} f_{\theta_q}^{\mathrm{wall}}(\theta) &= \frac{2\cos(\theta)\sin(\theta)}{1 - (1 - \Omega_1/2\pi)^2}, \\ f_{\psi_q}^{\mathrm{wall}}(\psi) &= 1/(2\pi). \end{aligned} \tag{7}$$

$\kappa_\nu(T_{\max})$ corresponds to the absorption coefficient of the point at maximum temperature, and $I_\nu^\circ(T_{\max})$ is its corresponding equilibrium intensity.

2.4. Numerical codes and coupling

The LES model for gaseous and solid phases presented in Sec. 2.2.1 has been implemented in the code AVBP [33]. This parallel CFD code, developed at CERFACS and IFPEN, solves the three-dimensional compressible Navier-Stokes equations on unstructured meshes. The third-order in space and time finite element TTGC scheme [34] is used. Navier-Stokes Characteristic Boundary Conditions (NSCBC,[35]) are used to prescribe the boundary conditions. The Tabulated Thermochemistry for Compressible flows formalism (TTC,[36]) is used to implement the flamelet model.

The in-house RAINIER code solves the radiative transfer equation in unstructured meshes using a Monte Carlo method. A Randomized Quasi Monte-Carlo [37] based on Sobol low-discrepancy sequences [38] is used for random numbers generation in order to increase the efficiency of the classical Monte Carlo Method [15]. As mentioned previously, ERM [16] is used for the calculation of the radiative power field, while OERM [32] is used for the calculation of the radiative directive fluxes at the probe positions. A statistical relative error of maximum 3% on radiative directive fluxes and radiative power calculation has been considered in the Monte-Carlo algorithm. In order to enhance convergence, points where radiative power is low are not converged with this accuracy. Indeed, if the RMS of the radiative power estimator is lower than 10 kW/m^3 (i.e. lower than 0.5% of maximum radiative power), the corresponding radiative power is considered as converged, since its weight in the final results is considered to be negligible.

Both codes, AVBP and RAINIER, are coupled using the Open-palm library [39]. The radiative power field is updated based on the temperature, burnt gases molar fractions (X_{CO_2} and X_{H_2O}) and soot volume fraction fields provided by the LES solver every N_{ite} iterations.

In order to determine the value of N_{ite}, two parameters, $\alpha_1(N)$ and $\alpha_2(N)$, are defined as L2 error norms of the radiative power and temperature fields:

$$\begin{aligned}\alpha_1(N) &= \sqrt{\int_V \left|T_{i_0+N} - T_{i_0}\right|^2 dV} \Bigg/ \sqrt{\int_V \left|T_{i_0}\right|^2 dV},\\ \alpha_2(N) &= \sqrt{\int_V \left|P^{\mathrm{R}}_{i_0+N} - P^{\mathrm{R}}_{i_0}\right|^2 dV} \Bigg/ \sqrt{\int_V \left|P^{\mathrm{R}}_{i_0}\right|^2 dV},\end{aligned} \tag{8}$$

where V corresponds to the computational domain volume, T_{i_0} and $P^{\mathrm{R}}_{i_0}$ are respectively instantaneous temperature and radiative power fields at a reference iteration i_0 of the fluid solver. T_{i_0+N} and $P^{\mathrm{R}}_{i_0+N}$ correspond to the temperature and radiative power fields at iteration $i_0 + N$, respectively. To choose the optimized N_{ite} value, the fields needed to calculate α_1 and α_2 are obtained in a preliminary study where the AVBP and RAINIER codes are fully coupled at each iteration.

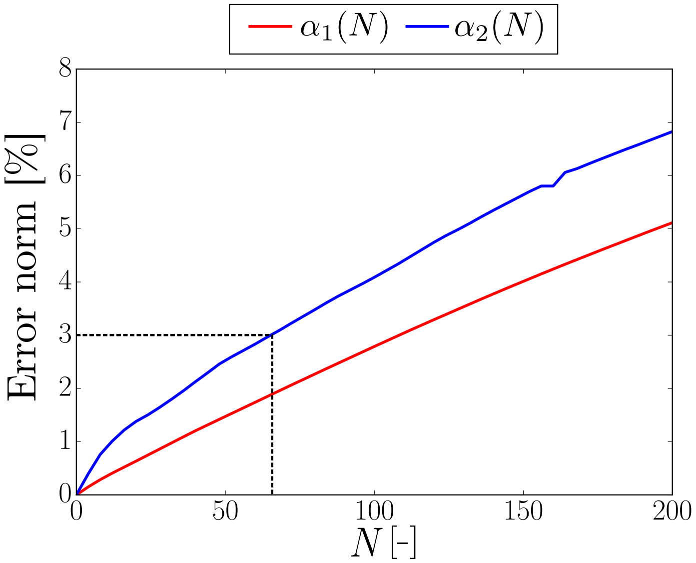

Figure 1. Evolution of L2 error norms of the temperature (red) and radiative power (blue) fields at fluid solver iteration $i_0 + N$ based on temperature and radiative power fields at fluid solver iteration i_0.

Figure 1 presents the evolution of $\alpha_1(N)$ and $\alpha_2(N)$ with the number of iterations of the fluid solver N. The $\alpha_1(N)$ profile shows that considering the reference temperature field T_{i_0} instead of the current field T_{i_0+N} yields a mean relative error around 1% for $N = 50$ up to 5% for $N = 200$. Similarly, the corresponding error of the computed radiative power field is denoted by the $\alpha_2(N)$ profile. The coupling iteration number N_{ite} satisfying $\alpha_2(N) = 3\%$ is $N_{\text{ite}} = 65$, and is here chosen for the coupled simulation. The time step of the LES solver is limited by the acoustic time scale (CFL criterion) and yields $\mathit{\Delta} t \approx 6.5 \times 10^{-8}$ s. The coupling period is then $\mathit{\Delta} t_{\text{cpl}} = 65\mathit{\Delta} t = 4.2 \times 10^{-6}$ s.

2.5. Numerical setup and CPU cost

The coupled simulation has been performed using a cluster equipped with Intel E5-2680 processors with a total computational time (including averaging time) of 1.5 million of CPU hours. The averaged fields have been computed over 250 ms of physical time. The breakdown of processors between both codes is 1120 CPU cores for the AVBP code and 1092 for the RAINIER code. Table 1 compares the relative CPU cost of the coupled simulation (MC) with two other simulations. The first one is an adiabatic simulation (ADIAB) where neither radiation nor soot particles descriptions have been considered. The second considers soot particles formation and radiation, which is described by the optically thin model (OPT,[17]). The latter is considered as reference for CPU cost. The combination of large-eddy simulation with the soot sectional model is already quite expansive. That is why the coupling with radiation through the Monte Carlo solver only yields a computational overhead of a factor 2.

Case	Soot description	Radiation description	Rel. CPU cost
ADIAB	None	None	1.0
OPT	Sectional	OPT	4.1
MC	Sectional	MC	8.2

Table 1. Relative CPU costs of the studied cases.

3. Results and validation

In the following, gaseous predictions with the coupled simulation (MC) are compared with experiments of [19] and [20] and the ADIAB and OPT computations. It must be first noted that experiments in [20] have been carried out in Albuquerque, where ambient pressure is equal to 0.84 bar, 17% lower than the pressure used in the computation (1.01325 bar). The soot volume fraction, soot intermittency and radiative intensity measurements by Shaddix et al. [19] have been done at Livermore, where ambient pressure is equal to 1 atm, justifying the choice to perform the simulations at 1 atm.

3.1. Instantaneous fields

Figure 2 shows the turbulent jet flame and the corresponding instantaneous fields of temperature (a), CO_2 (b) and H_2O (c) molar fractions and soot vol-

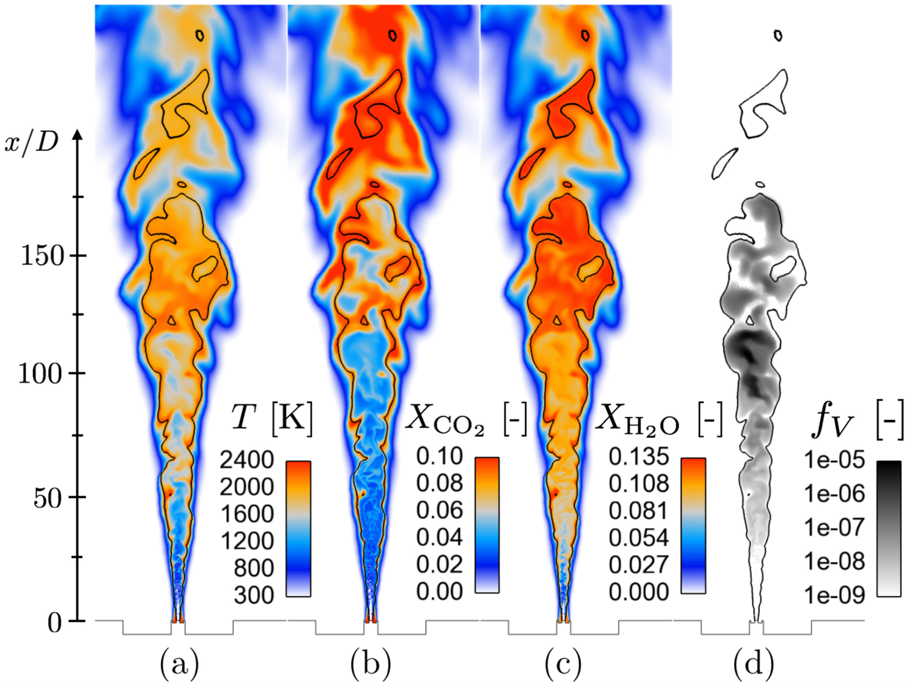

Figure 2. Instantaneous fields of, from left to right, temperature, CO_2 and H_2O molar fractions, and soot volume fraction. The stoichiometric isoline is also represented in black solid line.

ume fraction (d). On the one hand, the peaks in temperature and burnt gases concentrations are located along the stoichiomeric isoline of mixture fraction. On the other hand, soot particles are produced in the rich regions of the flame before being oxidized downstream. Then, different characteristics of radiative power can be expected depending on these different zones of the flame.

Figure 3 (a) shows the corresponding radiative power field computed by the Monte Carlo method. It results from the contribution of both gaseous and solid phases to the radiative transfer. The radiative power field computed from gaseous radiative properties only is shown in Figure 3 (b). As expected, its magnitude is correlated with peaks in temperature and burnt gases composition. However, the total field, Fig. 3 (a), additionally shows a significant effect of soot radiation where pockets of large soot volume fraction are localized. The

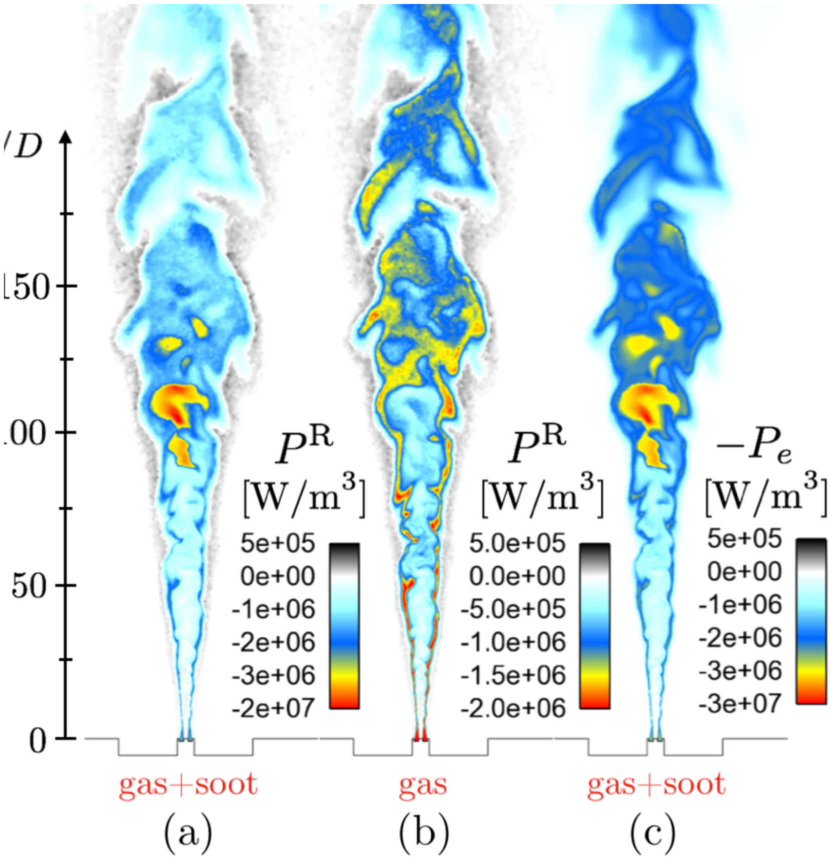

Figure 3. Instantaneous fields of, from left to right, radiative power accounting for both gas and soot contributions, radiative power only for gas contribution and emitted power accounting for both gas and soot contributions.

radiative field sent to the LES solver then accounts for the combination of both types of radiative transfer.

The field P^{R}, Fig. 3 (a), is mostly negative, indicating that emission is stronger than absorption in most regions. Positive values of radiative power can be seen downstream on the sides of the jet where cold burnt gases mix with the ambient air. Reabsorption phenomena are however not negligible at all as seen in Fig. 3 (c) where only the contribution $-P_e$ of the radiative emitted power is shown. The emission contribution is different from the total one in regions where soot or gaseous radiation dominate. Therefore, we can expect that an optically thin approximation will be quite inappropriate to describe thermal radiation on this flame.

3.2. Temperature and species profiles

Figure 4 presents the evolution of the axial temperature profiles for the three simulations. While for the first part of the flame, the temperature profiles are quite similar, the downstream temperature decrease is largely impacted by the hypothesis done for thermal radiation. The lowest decrease rate is obtained for the adiabatic computation where the peak of temperature corresponds to the average position of the stoichiometric mixture. Downstream this position, around $x = 200D$, turbulent mixing of hot burnt gases with ambient air cools the gases down. The highest decrease rate is obtained for the computation with the optically thin radiation model. This is due to the overestimated impact of radiative heat losses in the burnt gases. The coupled simulation (MC), which accounts for emission and reabsorption, presents lower radiative heat losses and, therefore, an intermediate temperature decrease rate between the other two simulations.

Figure 5 presents a comparison between mean and RMS radial profiles of temperature and species composition obtained at $x/D = 134$ for the three computations with experiments of Kearney et al. [20]. For all quantities in Fig. 5, a reasonable agreement is observed in terms of magnitude and shape. However, the difference in pressure prevents any definitive assessment of the validity for the reported profiles of Fig. 5. The fact that the optically thin model yields a better agreement with the experimental data is misleading and is due to compensating effects from the pressure mismatch. The temperature profiles for the three computations exhibit the same hierarchy as for the axial profiles in Fig. 4: the highest and lowest temperature are obtained for the computations without radiation and with the optically thin radiation model, respectively.

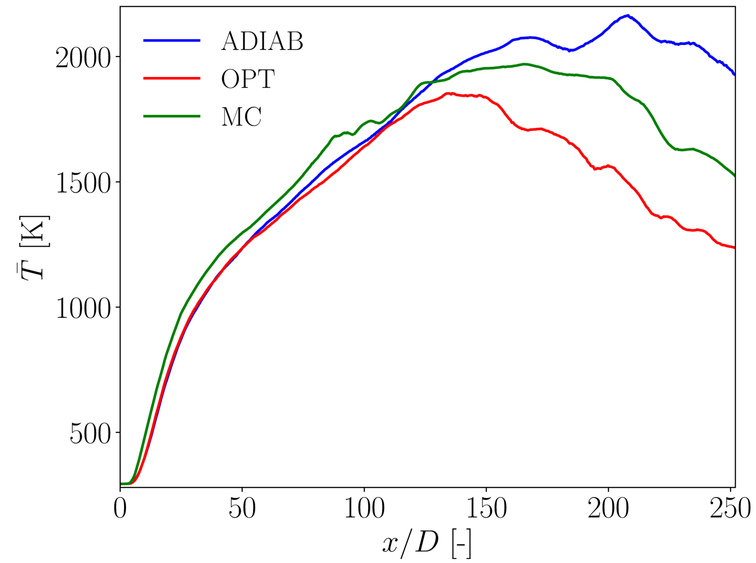

Figure 4. Mean temperature axial profiles for the different studied cases. Results obtained with adiabatic hypothesis (ADIAB), optically thin (OPT) [18] and coupled Monte-Carlo (MC) are represented in blue, red and green solid lines, respectively.

3.3. Soot volume fraction profiles

Figure 6 (a) presents a comparison of axial soot volume fraction profiles with experiments for MC and OPT simulations. While the peak is overestimated by a factor two and soot depletion due to oxidation is predicted too soon compared to experiments. The soot intermittency, shown in Fig. 6 (b) and defined as the probability of having soot volume fraction f_V lower than the experimental detection threshold $f_V^{\mathrm{th}} = 0.03$ ppm, is quite well reproduced by our model. Even if numerical results of soot intermittency seem slightly translated upstream, they globally confirm that the soot particle production dynamics is correctly reproduced. Similar discrepancies on the soot volume fraction between experimental and numerical results on other sooting jet flames have been observed by Mueller and Pitsch [24], whereas a previous work based on the DQMOM model presented an underestimation of the soot volume fraction for the currently studied flame [40]. In respect to state-of-the-art in large eddy simulations of soot

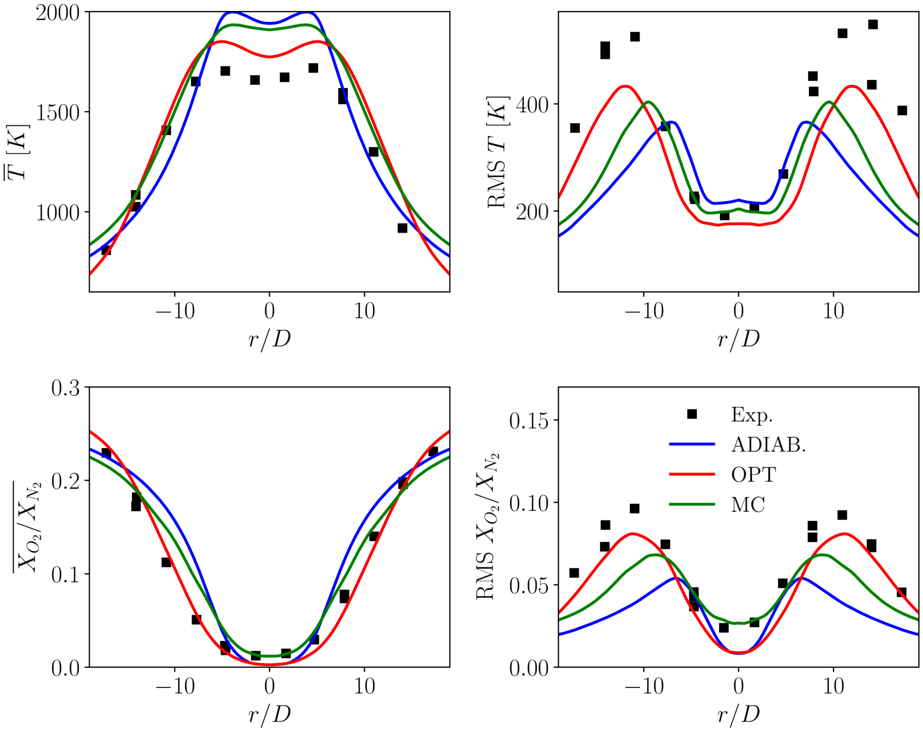

Figure 5. Mean (left) and RMS (right) radial profiles of temperature and species (X_{O_2}/X_{N_2}) for the different studied cases at $x/D = 134$. Results obtained with adiabatic hypothesis (ADIAB), optically thin (OPT) [18] and coupled Monte-Carlo (MC) are respectively represented in blue, red and green solid lines. Experimental measurements from [20] are presented in black squares.

production, the quality of the predictions can then be considered as satisfactory given the current uncertainties in soot modeling as discussed in [18].

Concerning radiation modeling, it can be observed that the detailed radiation description only slightly impacts the results for soot in Figs. 6 (a) and (b). The main difference concerns soot oxidation, which is predicted slightly later in the coupled simulation than in the optically thin radiation computation case. This can be explained by the fact that soot particles are formed and grow in rich regions, *i.e.* in the first half of the flame height, while radiation effects on the temperature field start appearing at $x/D = 130$ (see Fig. 4). Then, the soot formation and the main radiative heat losses occur in different regions so that soot production is only slightly impacted by radiation description. The coupled simulation results do not improve significantly the remaining disagreement between the numerical and experimental data. Achieving better soot predictions is then not related here to radiation modeling, but is rather impacted by the challenging uncertainties that remain in soot modeling. However, it should be noticed that the observed negligible effect of a detailed description of radiative transfer on soot prediction has to be considered as specific to this configuration and cannot be generalized to all turbulent sooting flames at this stage.

3.4. Radiant emission profiles

Figure 7(a) compares the axial profile of radiant emission profiles (Eq. 4) with the experimental measurements. The blue line corresponds to gaseous contribution from CO_2 and H_2O species whereas the red line corresponds to the total contribution when taking into account both gaseous and solid phases emissions. Figure 7(b) presents the radial profiles at different heights above the burner ($x/D = 50$, $x/D = 100$, $x/D = 135$ and $x/D = 175$). The first height, $x/D = 50$, corresponds to a zone with very low soot volume fraction. The second, $x/D = 100$, and fourth, $x/D = 175$, heights correspond to regions of moderate axial soot volume fraction (approximatively 0.1 ppm). Finally, the third one, $x/D = 135$ corresponds to a high axial soot volume fraction region (approximatively 1 ppm). Concerning the gaseous phase, for all these regions, CO_2 and H_2O species are present but the width of the flame jet increases with the height above the burner.

Looking at the results presented in Fig. 7(b), it can be observed that a fair agreement with the experiments is observed for the results with the total contribution, which is deemed good given the aforementioned uncertainties in soot production modelling. Comparing these results with those obtained for only the gaseous contribution, one can see that soot particles are an important contributor to the axial directive intensity for this flame. The discrepancies with the experimental results can be related to the differences observed in soot predictions. Indeed, the radial profiles of radiative intensity are well retrieved where soot radiation is negligible, i.e. where the soot volume fraction is low (full profile at $x/D = 50$ and profile at $x/D = 175$ for $r > 10D$).

For $x/D < 120$, the discrepancies on the predicted radiative intensity seem correlated with the disagreement on the axial profile of soot volume fraction (see Figs. 6 (a) and 7(a)). Initially, the amount of soot particles is underestimated, yielding a corresponding underestimation of the radiative intensity. Then, profiles of both soot volume fraction and radiative intensity are overpredicted. Hence, most of the discrepancies is consistent with uncertainties in the prediction of soot formation. However, the magnitude of disagreement in soot volume fraction in Fig. 6 (a) can reach up to a twofold factor while the disagreement in the peak of radiative intensity in Fig. 7(a) is much lower. This is because the radiative intensity is not only sensitive to the local predictions on the centerline. As it will be discussed in Sec. 4.1, soot radiation is here mainly optically thin so that the radiative intensity is in fact sensitive to the total thickness of soot i.e. the total volume of soot material crossed by photon rays. The ratio of line-of-sight integrated soot volume fraction between numerical results and experimental data is shown in Fig. 8(a). The soot thickness is seen to be mostly underestimated everywhere except for a mild overestimation around $x/D = 120$.

Knowing that soot and gas radiations barely interact (see Sec. 4.1), the soot contribution to the compared radiative intensity is estimated by subtracting the gaseous radiation results from the fully coupled results and the experimental data. The ratio between numerical results and experimental data is shown in the figure 8(b). Figures 8(a) and 8(b) demonstrate that the discrepancies between soot thickness and soot radiation are strongly correlated. The volume of soot particles is underestimated for $x/D < 120$ consistently with Fig. 8(b) and the corresponding Figs. 7(a) and 7(b) at $x/D = 100$. At $x/D = 135$, a correct yet slightly overestimated magnitude of soot thickness is observed, which is again consistent with Fig. 8(b) and the corresponding Fig. 7(a) and 7(b) at x/D =

135. However, while good results are obtained at $x/D = 175$ in Fig. 7(b), figure 8(a) instead indicates an underestimation of the total soot volume. This inconsistently good results for radiative intensity at $x/D = 175$ is probably the sign of radiation modeling errors that are at play such as the radiative properties attributed to the soot aggregates.

Figure 9 presents the spectral distribution of volumetric emitted power P_e from soot and gas at different points of the jet centerline. Horizontal lines denote the total emitted power from soot and gas at the considered points. The gas emission spectrum is highly dynamic and composed of very intense bands at low wavenumbers, whereas the soot emission spectrum is continuous and is more intense for high wavenumbers. Depending on the position, the major contributor in emitted power can be either the gas or the soot phase. This is because gas and soot particles spectra present different characteristics and diverse radiative behaviours can be expected depending on the considered position in the flame. The net effect for the volume integrated quantities is investigated in the next section before studying turbulence-radiation interactions.

4. Analysis

4.1. Absorption and emission contributions on radiative power

In this section, in order to investigate the role of gaseous participating species and soot particles in the total volume integrated radiative power, one representative instantaneous field has been post-processed with the MC solver by considering four different situations: gas emission and gas absorption (**GEGA**); gas emission and soot absorption (**GESA**); soot emission and gas absorption (**SEGA**); soot emission and soot absorption (**SESA**). For these computations, as the role of soot particles and gaseous participating species are not symmetric in emission and absorption, the ERM calculation based on the reciprocity principle is not consistent and a backward Monte Carlo method is used instead. The transmissivity of both phases is always considered in the four computation cases.

Table 2 presents the corresponding total volume integrated emitted power (P_e), absorbed power (P_a) and radiative power (P^{R}) for the four computations, compared with the reference computation (case **Ref.**), where gaseous and soot contributions are considered for both emission and absorption. For this instantaneous solution, several observations can be done:

- Approximatively 56% (6.06 kW) of the emitted power from the gaseous phase (10.86 kW) is reabsorbed by the gaseous phase,
- Less than 0.5% (0.03 kW) of the emitted power from the gaseous phase (10.86 kW) is reabsorbed by the soot phase,
- Approximatively 10% (0.13 kW) of the emitted power from the soot phase (1.27 kW) is reabsorbed by the soot phase,
- Less than 2% (0.02 kW) of the emitted power from the soot phase (1.27 kW) is reabsorbed by the gaseous phase,
- Even if in the regions of high soot volume fraction soot particles are the major contributors to radiative transfer, soot particles only account for 21 % of the total volume integrated radiative power due to the strong spatial localization of soot ligaments compared to the region occupied by the most radiative gaseous species, as it can be observed in Fig. 2.

Case	Ref.	GEGA	GESA	SESA	SEGA
P_e [kW]	12.13	10.86	10.86	1.27	1.27
P_a [kW]	6.24	6.06	0.03	0.13	0.02
P^{R} [kW]	-5.89	-4.80	-10.83	-1.14	-1.25

Table 2. Gaseous and soot contributions on emitted and absorbed powers integrated on the whole computational domain.

Reabsorption phenomena are more important for the gaseous phase than for the solid phase in the investigated flame. Indeed, reabsorption only slightly modifies soot total contribution to radiative power (0.15 kW out of 1.27 kW). More-over, very small interactions are observed between soot particles and gaseous species in terms of radiative transfer. Indeed, soot only slightly absorbs gaseous emission (0.03 kW out of 10.86 kW), and gas absorbs little of soot emission (0.02 kW out of 1.27 kW). Several of these results along with the global level of reabsorption for gas and soot contributions are very well in line with previous results from Mehta *et al.* [41] for atmospheric ethylene jet flames: 50% of reabsorption for burnt gases, 10% for soot.

The corresponding spectral volume-integrated emission and absorption of the different cases are presented in Fig. 10. Two cK bands from CO_2 radiative properties are the major contributors to gaseous emissions (from 2000 to 2500 cm^{-1}). For these bands, important gas absorption is also observed (see case GEGA). For soot particles, soot absorption coefficient presents a continuous wide band spectrum and lower reabsorption for soot particles is observed (see cases GESA and SESA). Finally, gaseous reabsorption from soot emission is negligible and is only observed for the two bands mostly responsible for gaseous emissions (see case SEGA).

It can then be concluded that the radiative exchanges between gas and solid phases are here negligible. Regarding the gaseous and soot reabsorption, one can interpret these results by looking at the optical thicknesses for each spectral band and at different positions above the injector. To do so, we consider $\tau_\nu(x)$ the transmissivity for each height x above the burner and the considered narrow band centered around ν. The transmissivity of the heterogeneous column is computed following the cK model.

Figure 11 presents the corresponding transmissivities at three different positions above the burner: $x/D = 62.5$, $x/D = 125.0$ and $x/D = 187.5$. The first and third positions correspond to regions of low mean soot volume fraction (lower than 0.1 ppm) whereas the second corresponds to a region of maximum axial mean soot volume fraction (higher than 1 ppm). For the range of temperatures between 300 K and 1 900 K observed in the flame, the considered range of wavenumbers [150 cm^{-1},10 000 cm^{-1}] accounts for at least 95% of the radiative power. The considered limit of an optically thin medium ($\tau_\nu \approx e^{-0.1}$)

is also presented with an horizontal dashed line. For all these three heights, transmissivities taking into account gas, soot and gas+soot contributions are plotted.

First, concerning gas emissions, it can be observed that the two bands highly contributing to gas emission present transmissivities largely lower than $e^{-0.1}$, explaining then why for these two bands, reabsorption is significative, and therefore, total gas reabsorption is important.

Secondly, it can be seen that soot particles have a strong influence at $x/D = 125.0$ where soot volume fraction is maximum. The transmissivity across soot particles decreases with the wavenumber. However, it can be observed that the optical thickness of soot particles is lower than those of the two highly contributing bands ones. This explains why only 10 % of the soot emitted power is reabsorbed.

Finally, for $x/D = 62.5$ and $x/D = 187.5$, which correspond to regions with low soot volume fraction, the soot phase does not impact the transmissivity spectrum across the flame.

4.2. Total turbulence-radiation interactions (TRI)

In order to investigate TRI, Fig. 12 presents a comparison between the mean fields of radiative power from the coupled simulation and the one obtained from the resolution of the RTE based on mean fields of temperature, pressure, CO_2 and H_2O molar fractions and soot volume fraction. This latest simulation corresponds to the results obtained when neglecting turbulence-radiation interactions (TRI) in a RANS simulation. One can observe that when accounting for large-scale turbulence-radiation interactions (solved within coupled LES approach), the radiative power in the region of soot presence ($-10 < r/D < 10$ and $100 < x/D < 175$) is largely reduced.

It is important to outline that the present observation relies on the resolved scales captured on the LES mesh. In reality, any instantaneous field φ is composed of a resolved and subgrid components: $\varphi = \varphi_{\text{les}} + \varphi_{\text{sgs}}$. The complete evaluation of turbulence-radiation interactions should then be based on the radiative power computed from the instantaneous and entire 3D fully-resolved turbulent fields of composition $\xi = (X_{CO_2}, X_{H_2O}, f_V)$ and temperature to quantify how much $\overline{P^R(\xi,T)}$ differs from $P^R\left(\overline{\xi},\overline{T}\right)$. This is different from the difference between $\overline{P^R(\xi_{les},T_{les})}$ and $P^R\left(\overline{\xi_{les}},\overline{T_{les}}\right)$ shown in Fig. 12. While one can safely consider that $\overline{\xi_{les}} = \overline{\xi}$ and $P^R\left(\overline{\xi},\overline{T}\right) = P^R\left(\overline{\xi_{les}},\overline{T_{les}}\right)$, the complete determination of the mean radiative power should include a subgrid-scale contribution:

$$\overline{P^R(\xi,T)} = \overline{P^R(\xi_{les},T_{les})} + \overline{P^R_{sgs}}. \tag{9}$$

In the present study, subgrid-scale modeling in the description of radiative transfer has been neglected. However, as shown in Fig. 6, soot production is characterized by a strong intermittency that may greatly contribute to the subgrid-scale radiative power. Therefore, the soot subgrid models, accounting for the unresolved soot intermittency, could strongly affect the numerical predictions of TRI. Very few studies exist on soot subgrid models [42, 25] and the quantification of their impact on TRI will require a dedicate study that is out of the scope of this work. In the following of Sec. 4.2, the notation φ_{les} is dropped and φ is considered instead for the sake of clarity while bearing in mind that neglecting subfilter-scale TRI is consistent with the retained hypothesis of the coupled LES setup but most likely impacts the reported results for the investigated flame.

Spatial integration of both fields from Fig. 12 over the computational domain yields 5.7 kW for the coupled simulation and 5.0 kW for the simulation based on the mean fields of temperature, pressure, CO_2 and H_2O molar fractions, and soot volume fraction, respectively. A non-negligible impact of turbulence-radiation interactions is then observed with an increase of 14% of the total radiative power (0.7 kW), while much larger discrepancies are seen locally in Fig. 12. This justifies the interest in unsteady coupled simulations based on an LES approach in order to correctly capture the large-scale turbulence-radiation interactions.

Figure 13 compares the radiative intensity profiles similar to Fig. 7(a) when considering only gas contribution and when considering both gas and solid phase contributions in radiative heat transfer. Two sets of curves are shown: mean profiles from coupled LES results and profiles computed from mean fields directly. The difference between profiles for gas-only radiative intensities indicates that turbulence-radiation interactions fairly increase mean radiative intensities in gas phase, as already observed in the literature [8, 2, 10, 43, 44]. Looking at the total radiative intensities that additionally account for soot particles, one can observe that the profile estimated from mean fields significantly overestimates the mean LES result in the sooting region. Therefore, turbulence-radiation interactions effects slightly increase the radiative power contribution from burnt gases while they significantly decrease the one from soot particles. This observation for the studied flame has also been seen in the work of [13, 45] in computations of three ethylene/air and one oxygen-enriched/propane diffusion flames where soot absorption coefficient-Planck function correlation and absorption turbulence-radiation interactions have been studied. Consalvi and Nmira have observed negative correlations in these quantities, explaining a decrease in the radiative power.

In order to distinguish the emitted and absorption contributions to the total turbulence-radiation interactions, the mean radiative power $\overline{P^{\mathrm{R}}}$ is written as

$$\begin{aligned}\overline{P^{\mathrm{R}}} &= \int_{\nu=0}^{+\infty}\int_{4\pi}\left(\overline{\kappa_\nu I_\nu} - \overline{\kappa_\nu I_\nu^\circ}\right) d\Omega d\nu \\ &= \underbrace{\int_{\nu=0}^{+\infty}\int_{4\pi}\overline{\kappa_\nu I_\nu} d\Omega d\nu}_{\overline{P_a}} - \underbrace{\int_{\nu=0}^{+\infty}\int_{4\pi}\overline{\kappa_\nu I_\nu^\circ} d\Omega d\nu}_{\overline{P_e}}\end{aligned} \tag{10}$$

where $\overline{P_a}$ and $\overline{P_e}$ are respectively the mean absorbed and emitted powers.

With $\overline{\xi} = (\overline{X_{CO_2}}, \overline{X_{H_2O}}, \overline{f_V})$, the mean absorbed and emitted powers can be written as

$$\begin{aligned}\overline{P_a} &= \underbrace{\int_{\nu=0}^{+\infty}\int_{4\pi}\kappa_\nu(\overline{T},\overline{\xi})I_\nu(\overline{T},\overline{\xi}) d\Omega d\nu}_{\widehat{P_a}:\ \text{no TRI}} \\ &+ \underbrace{\int_{\nu=0}^{+\infty}\int_{4\pi}\left(\overline{\kappa_\nu I_\nu} - \kappa_\nu(\overline{T},\overline{\xi})I_\nu(\overline{T},\overline{\xi})\right) d\Omega d\nu,}_{P_a^{\mathrm{TRI}}:\ \text{absorption TRI}}\end{aligned} \tag{11}$$

$$\begin{aligned}\overline{P_e} &= \underbrace{\int_{\nu=0}^{+\infty}\int_{4\pi} \kappa_\nu(\overline{T},\overline{\xi}) I_\nu^\circ(\overline{T}) d\Omega d\nu}_{\widehat{P_e}\text{: no TRI}} \\ &+ \underbrace{\int_{\nu=0}^{+\infty}\int_{4\pi} \left(\overline{\kappa_\nu I_\nu^\circ} - \kappa_\nu(\overline{T},\overline{\xi}) I_\nu^\circ(\overline{T})\right) d\Omega d\nu}_{P_e^{\mathrm{TRI}}\text{: emission TRI}},\end{aligned} \tag{12}$$

where $I_\nu(\overline{T},\overline{\xi})$ denotes the spectral radiative intensity computed from the 3-D mean fields. $\widehat{P_a}$ and $\widehat{P_e}$ are the corresponding absorbed and emitted power, respectively. The additional terms due to turbulence-radiation interactions are P_a^{TRI} and P_e^{TRI}.

Figure 14 presents axial profiles of these different contributions. As observed in radiative intensity profiles, high increase of emitted power can be observed from $x/D = 100$ corresponding to the presence of high soot volume fraction. Maximum emitted power is observed at $x/D \approx 125$ corresponding to maximum soot volume fraction. Then, for $x/D \in [125, 200]$, soot volume fraction and therefore emitted power decrease. The emitted power beyond $x/D = 200$ is mainly due to CO_2 and H_2O products. In all the region of soot presence ($x/D \in [100, 200]$), the emitted turbulence-radiation interactions (P_e^{TRI}) are important (approximatively one-third of $\widehat{P_e}$) and negative, while it is positive for lower and higher x/D values. Concerning absorbed power ($\widehat{P_a}$), high contribution (approximatively half of $\widehat{P_e}$) in total radiative power is observed in gaseous-only regions ($x/D < 100$ and $x/D > 200$) while its contribution is lower in soot regions, which is consistent with the analysis in Sec. 4.1 for the studied jet flame. Finally, positive absorbed turbulence-radiation interactions (P_a^{TRI}) are observed all over the flame height with a small magnitude.

Table 3 gives the volume integral values of emitted, absorbed and total radiative powers accounting for TRI ($\overline{P_e}$, $\overline{P_a}$ and $\overline{P^{\mathrm{R}}}$), without accounting for TRI ($\widehat{P_e}$, $\widehat{P_a}$ and $\widehat{P_a} - \widehat{P_e}$) and the corresponding TRI contributions (P_e^{TRI}, P_a^{TRI} and $P_a^{\mathrm{TRI}} - P_e^{\mathrm{TRI}}$). Due to the narrow location of the soot particles in the jet flame, TRI globally account only for 13% of total emitted power and 14 % of total absorbed power. However, the local effects can be much larger, which could be significant in other configurations.

Type	With TRI [kW]	Without TRI [kW]	TRI [kW]	TRI [%]
Emitted	11.3	9.8	1.5	13
Absorbed	5.6	4.8	0.8	14
Total	-5.7	-5.0	-0.7	12

Table 3. TRI contributions on volume integrated emitted, absorbed and total radiative powers.

4.3. Closure of TRI effects on the mean emitted radiative power

The closure of P_a^{TRI} depends on the temporal correlation between the local instantaneous absorption coefficient and the radiative intensity determined by the entire 3-D instantaneous field. This non-local relationship makes a general model formulation complex and is not addressed here. On the other hand, the TRI contribution P_e^{TRI} on the mean emitted radiative power, which is here the major part, is determined by local average quantities, which makes a model formulation from Taylor series possible [2, 44].

Noting κ_{Pl} the Planck mean absorption coefficient, $\overline{\kappa_{\mathrm{Pl}}}$ its mean value, κ'_{Pl} its fluctuation, and T' the temperature fluctuation, the mean emitted power $\overline{P_e}$ can be expressed as

$$\begin{aligned} \overline{P_e} &= 4\sigma\overline{\kappa_{\mathrm{Pl}}T^4} \\ &= 4\sigma\overline{\kappa_{\mathrm{Pl}}}\,\overline{T}^4\left(1 + 6\frac{\overline{T'^2}}{\overline{T}^2} + 4\frac{\overline{\kappa'_{\mathrm{Pl}}T'}}{\overline{\kappa_{\mathrm{Pl}}}\,\overline{T}}\right). \end{aligned} \tag{13}$$

Let us introduce $\kappa_{\mathrm{Pl}} = \kappa_{\mathrm{Pl}}^{\mathrm{gas}} + \kappa_{\mathrm{Pl}}^{\mathrm{soot}}$ with $\kappa_{\mathrm{Pl}}^{\mathrm{gas}}$ and $\kappa_{\mathrm{Pl}}^{\mathrm{soot}}$ respectively the gas and soot contributions to the total Planck mean absorption coefficient κ_{Pl}.

Equation (13) can then be written as:

$$\begin{aligned}\overline{P_e} = {} & \underbrace{4\sigma\overline{\kappa_{\mathrm{Pl}}^{\mathrm{gas}}}\,\overline{T}^4\left(1+6\frac{\overline{T'^2}}{\overline{T}^2}+4\frac{\overline{\kappa_{\mathrm{Pl}}^{\mathrm{gas}\prime}T'}}{\overline{\kappa_{\mathrm{Pl}}^{\mathrm{gas}}}\,\overline{T}}\right)}_{\overline{P_e^{\mathrm{gas}}}} \\ & + \underbrace{4\sigma\overline{\kappa_{\mathrm{Pl}}^{\mathrm{soot}}}\,\overline{T}^4\left(1+6\frac{\overline{T'^2}}{\overline{T}^2}+4\frac{\overline{\kappa_{\mathrm{Pl}}^{\mathrm{soot}\prime}T'}}{\overline{\kappa_{\mathrm{Pl}}^{\mathrm{soot}}}\,\overline{T}}\right)}_{\overline{P_e^{\mathrm{soot}}}}.\end{aligned} \tag{14}$$

The difference due to TRI between the Planck mean absorption coefficient and the Planck absorption coefficient computed from mean fields is quantified as:

$$\begin{aligned}\overline{\kappa_{\mathrm{Pl}}^{\alpha}} &= \kappa_{\mathrm{Pl}}^{\alpha}(\overline{T},\overline{\xi}) + \left(\overline{\kappa_{\mathrm{Pl}}^{\alpha}} - \kappa_{\mathrm{Pl}}^{\alpha}(\overline{T},\overline{\xi})\right) \\ &= \kappa_{\mathrm{Pl}}^{\alpha}(\overline{T},\overline{\xi})\left[1+\frac{\overline{\kappa_{\mathrm{Pl}}^{\alpha}} - \kappa_{\mathrm{Pl}}^{\alpha}(\overline{T},\overline{\xi})}{\kappa_{\mathrm{Pl}}^{\alpha}(\overline{T},\overline{\xi})}\right]\end{aligned} \tag{15}$$

where α stands for $\{\mathrm{gas,soot}\}$ and $\overline{\kappa_{\mathrm{Pl}}^{\alpha}}$ is the corresponding Planck mean absorption coefficient. For the soot phase with the considered soot absorption coefficient (Eq. (1)), Equation (15) can be simplified. Indeed, $\kappa_{\mathrm{Pl}}^{\mathrm{soot}}(T,\xi)$ can first be directly computed as a function of soot volume fraction f_V and temperature T:

$$\kappa_{\mathrm{Pl}}^{\mathrm{soot}}(T,\xi) = \frac{\sum_{n=1}^{+\infty} 24/n^5}{\sum_{n=1}^{+\infty} 6/n^4}\frac{C_0 f_V T}{C_2} \approx 3.83\frac{C_0 f_V T}{C_2} \tag{16}$$

where $C_2 = hc/k_B$ is the second Planck constant. Equation (15) for $\overline{\kappa_{\mathrm{Pl}}^{\mathrm{soot}}}$ can then be determined analytically as:

$$\overline{\kappa_{\mathrm{Pl}}^{\mathrm{soot}}} = 3.83\frac{C_0\overline{f_V}\,\overline{T}}{C_2}\left(1+\frac{\overline{f_V' T'}}{\overline{f_V}\ \overline{T}}\right), \tag{17}$$

and, considering only the lowest order terms in the truncation series, $\overline{P_e^{\mathrm{soot}}}$ is expressed directly as:

$$\overline{P_e^{\mathrm{soot}}} = \underbrace{\frac{15.32C_0}{C_2}\sigma\overline{f_V}\ \overline{T}^4}_{\widehat{P_e^{\mathrm{soot}}}}\left(1+10\frac{\overline{T'^2}}{\overline{T}^2}+5\frac{\overline{f_V' T'}}{\overline{f_V}\ \overline{T}}\right). \tag{18}$$

Finally, Equation (14) is written as:

$$\begin{aligned}\overline{P_e} = \widehat{P_e^{\mathrm{gas}}} \quad & \times \left(1 + \frac{\overline{\kappa_{\mathrm{Pl}}^{\mathrm{gas}}} - \kappa_{\mathrm{Pl}}^{\mathrm{gas}}(\overline{T}, \overline{X_{\mathrm{CO}_2}}, \overline{X_{\mathrm{H}_2\mathrm{O}}})}{\kappa_{\mathrm{Pl}}^{\mathrm{gas}}(\overline{T}, \overline{X_{\mathrm{CO}_2}}, \overline{X_{\mathrm{H}_2\mathrm{O}}})}\right) \\ & \times \left(1 + 6\frac{\overline{T'^2}}{\overline{T}^2} + 4\frac{\overline{\kappa_{\mathrm{Pl}}^{\mathrm{gas}\prime} T'}}{\overline{\kappa_{\mathrm{Pl}}^{\mathrm{gas}}}\,\overline{T}}\right) \\ + \widehat{P_e^{\mathrm{soot}}} \quad & \times \left(1 + 10\frac{\overline{T'^2}}{\overline{T}^2} + 5\frac{\overline{f_V' T'}}{\overline{f_V}\,\overline{T}}\right).\end{aligned} \tag{19}$$

Figures 15 and 16 present the axial profiles of the different terms in TRI factors appearing in Eq. (19) for the gas and soot phases respectively.

Regarding the gaseous phase, the predominant term corresponds to temperature fluctuations (term $6\frac{\overline{T'^2}}{\overline{T}^2}$). The two other terms are positive or negative depending on the position in the flame, and have a smaller contribution.
In the soot emission contribution, despite the fact that temperature fluctuations alone have a non-negligible impact, the main term corresponds to the soot volume fraction - temperature fluctuations correlation. This term is positive for $x/D < 75$ and $x/D > 200$ while it is negative for $x/D \in [75, 200]$ corresponding to the regions of high soot volume fraction.

Based on the closure modeled proposed in Eq. (19), Figure 17 compares the axial profiles of the mean emitted power from gas and soot phases. Very good agreement is achieved by the derived model for the mean emitted power. Results for the gaseous phase contribution are excellent while some discrepancies are observed for the modeled mean emitted power from soot. This is attributed to the high intermittency of soot production in this flame (as detailed in [18]), which makes the retained truncation of the Taylor series less acurrate.

Figure 18 presents a comparison between exact (from coupled LES) and modeled axial profiles of total emitted power TRI contribution only. The good reproduction of the TRI effects is again retrieved with the proposed closure model.

Integrating Eq. (19) over the computational volume, one can define the total powers of the different terms responsible for gas and soot emission TRI:

$$
\begin{aligned}
&(1\text{a}) &&= \int_V \widehat{P_e^{\text{gas}}}\, dV \\
&(1\text{b}) &&= \int_V \widehat{P_e^{\text{gas}}} \left(\frac{\overline{\kappa_{\text{Pl}}^{\text{gas}}} - \kappa_{\text{Pl}}^{\text{gas}}(\overline{T}, \overline{\xi^{\text{gas}}})}{\kappa_{\text{Pl}}^{\text{gas}}(\overline{T}, \overline{\xi^{\text{gas}}})} \right) dV \\
&(1\text{c}) &&= \int_V \widehat{P_e^{\text{gas}}} \left(1 + \frac{\overline{\kappa_{\text{Pl}}^{\text{gas}}} - \kappa_{\text{Pl}}^{\text{gas}}(\overline{T}, \overline{\xi^{\text{gas}}})}{\kappa_{\text{Pl}}^{\text{gas}}(\overline{T}, \overline{\xi^{\text{gas}}})} \right) 6 \frac{\overline{T'^2}}{\overline{T}^2} dV \\
&(1\text{d}) &&= \int_V \widehat{P_e^{\text{gas}}} \left(1 + \frac{\overline{\kappa_{\text{Pl}}^{\text{gas}}} - \kappa_{\text{Pl}}^{\text{gas}}(\overline{T}, \overline{\xi^{\text{gas}}})}{\kappa_{\text{Pl}}^{\text{gas}}(\overline{T}, \overline{\xi^{\text{gas}}})} \right) 4 \frac{\overline{\kappa_{\text{Pl}}^{\text{gas}\prime} T'}}{\overline{\kappa_{\text{Pl}}^{\text{gas}}}\, \overline{T}} dV \\
&(2\text{a}) &&= \int_V \widehat{P_e^{\text{soot}}}\, dV \\
&(2\text{b}) &&= \int_V \widehat{P_e^{\text{soot}}}\, 10 \frac{\overline{T'^2}}{\overline{T}^2} dV \\
&(2\text{c}) &&= \int_V \widehat{P_e^{\text{soot}}}\, 5 \frac{\overline{f_V' T'}}{\overline{f_V}\, \overline{T}} dV
\end{aligned}
\tag{20}
$$

where $\overline{\xi^{\text{gas}}} = (\overline{X_{\text{CO}_2}}, \overline{X_{\text{H}_2\text{O}}})$.

Total	11.3 kW						
Phase	Gas				Soot		
Per phase	10.4 kW (92%)				0.94 kW (8%)		
	(1a)	(1b)	(1c)	(1d)	(2a)	(2b)	(2c)
[kW]	8.1	-0.70	3.0	0.074	1.9	0.25	-1.2
%	71.0	-6.1	26.3	0.6	16.7	2.2	-10.5

Table 4. Gaseous and soot contributions on emitted power TRI.

There corresponding values are given in Tab. 4. It is first observed that temperature fluctuations alone are responsible for a positive TRI for both gaseous and soot phases. A negative TRI effect is observed due to the cross-correlation between soot volume fraction and temperature, whereas a positive impact of gaseous absorption coefficient and temperature cross-correlation is obtained. For the gaseous phase, the positive temperature fluctuation term is the one responsible for the major part of TRI effects (+37%). This effect is slightly mitigated by the TRI effects on $\overline{\kappa_{\text{Pl}}^{\text{gas}}}$, denoted by $(1b)$. The total increase of mean emitted power from the gaseous phase due to TRI effects is then finally +29%. On the other hand, for the soot phase, the negative cross-correlation between temperature and soot volume fraction is the one responsible for the major part of TRI effect (-63%). The total decrease of mean emitted power for the soot phase due to TRI is -50%. The global net effects of TRI from all sources is +14% on the integrated mean emitted power. It is the result of opposite contributions from gaseous and soot TRI effects.

4.4. Indication of soot dynamics impact on temperature root-mean-square

Figure 5 indicates larger values of temperature root-mean-square (T_{rms}) at the height $x/D = 134$ in both cases considering thermal radiation. This is actually confirmed at other heights. Such a feature is quite surprising since thermal radiation would be believed to homogenize the instantaneous field and reduce T_{rms}. The interpretation of the results is however not trivial since the different simulations exhibit different local mixture fraction and mean temperature due to the varied description of heat transfer that impacts directly the temperature field, and indirectly the density field and jet spreading rate. Besides, all these effects cumulate along the jet height. In order to isolate the variation in T_{rms} as much as possible from these perturbations, radial profiles are recast into relative magnitude of T_{rms} in respect to the local mean temperature which is plotted as a function of the mean mixture fraction. The results are shown in Fig. 19 for the different considered heights. The blacked dashed curve represents the soot turbulent intensity in the coupled Monte Carlo simulation that is discussed later.

The same trends as observed directly as function of radial coordinate (not shown) are confirmed: the coupled Monte Carlo simulations and also the LES results with an optically thin approximation for radiation show notably larger peaks in temperature rms, signifying a stronger level of magnitude in turbulent temperature fluctuations. The varying mean mixture fraction and mean temperature do not introduce any artifact in the observation. The fact that similar trends are obtained for the optically thin and detailed radiation models indicate that the increase in T_{rms} is not related to the introduced Monte Carlo statistical error either.

A better understanding can be obtained by considering the radiative source term that appears in the balance equation for the enthalpy root-mean-square [46], related to the correlation between the radiative power and temperature:

$$\overline{h'P^{R'}} \propto \overline{T'P^{R'}} = \overline{T'P'_a} - \overline{T'P'_e} \tag{21}$$

As the described phenomenon might occur due to the soot contribution that is here dominated by emission, and since a similar behavior is observed in the optical thin radiation case, the correlation term between emitted power and temperature should explain alone the increased T_{rms}. Closing this term similarly as others in Sec. 4.3, one can write

$$\begin{aligned} \overline{T'P'_e} &= 4\sigma\overline{\kappa_{\mathrm{Pl}}^{\mathrm{gas}}}\,\overline{T}^5\left(4\frac{\overline{T'^2}}{\overline{T}^2} + \frac{\overline{\kappa_{\mathrm{Pl}}^{\mathrm{gas}'}T'}}{\overline{\kappa_{\mathrm{Pl}}^{\mathrm{gas}}}\,\overline{T}}\right) \\ &+ 4\sigma\overline{\kappa_{\mathrm{Pl}}^{\mathrm{soot}}}\,\overline{T}^5\left(4\frac{\overline{T'^2}}{\overline{T}^2} + \frac{\overline{\kappa_{\mathrm{Pl}}^{\mathrm{soot}'}T'}}{\overline{\kappa_{\mathrm{Pl}}^{\mathrm{soot}}}\,\overline{T}}\right) \end{aligned} \tag{22}$$

In the absence of soot, only the first term on the right-hand-side remains. The dependency of the mean Planck absorption coefficient on temperature can be approximated as

$$\frac{\kappa_{\mathrm{Pl}}^{\mathrm{gas}'}}{\overline{\kappa_{\mathrm{Pl}}^{\mathrm{gas}}}} \approx \alpha\frac{T'}{\overline{T}} \tag{23}$$

where α is mostly negative in burnt gases [26], peaking at maximum to -2.5 for $\mathrm{H_2O}$ at 2500 K. The gaseous temperature-absorption-coefficient correlation is then negative, but the net gaseous contribution to $\overline{T'P'_e}$ remains positive, yielding an a priori expected behaviour: a negative source term in the enthalpy rms transport equation makes T_{rms} decrease. The contrary is however here observed because of the soot contribution, second term in Eq. (22). With the Rayleigh model for soot radiative properties, the correlation between temperature and soot mean-Planck absorption coefficient is given by:

$$\overline{\kappa_{\mathrm{Pl}}^{\mathrm{soot}'} T'} = 3.83 \frac{C_0 \overline{f_V}\, \overline{T}^2}{C_2} \left(\frac{\overline{T'^2}}{\overline{T}^2} + \frac{\overline{f_V' T'}}{\overline{f_V}\, \overline{T}} \right) \tag{24}$$

The significant relative magnitude of fluctuations in soot volume fraction is shown in Fig. 19: it is almost everywhere larger than 100% and can peak beyond 400%. When combined with the negative nature of the correlation between temperature and soot volume fraction that was previously highlighted, this yields a notable negative contribution $\overline{\kappa_{\mathrm{Pl}}^{\mathrm{soot}'} T'}$ to the term $\overline{T' P_e'}$, which eventually changes its sign given the large magnitude of soot volume fraction fluctuations. This explanation finally introduces a positive source term in the balance equation of enthalpy rms, leading to an increase in T_{rms}. Figure 3 confirms that the peaks of increased T_{rms} and the ones of soot volume fraction rms are undoubtedly connected. While this scenario will have to be further investigated in the future, the present coupled results indicate an original effect of soot dynamics on temperature fluctuations through thermal radiation.

5. Conclusion

Radiative heat transfer is studied in a coupled simulation of a turbulent and sooted jet diffusion flame. The modelling strategy combines state-of-the-art approaches: large-eddy simulation of reactive flows, a detailed sectional model for soot formation, a Monte-Carlo resolution of the radiative transfer equation with the accounting of spectral radiative properties for both gaseous and solid (soot particles) phases. The achieved detailed methodology is validated against experimental data, yielding an overall good prediction in respect to the present state-of-the-art. The obtained agreement in terms of temperature, species and soot volume fraction is satisfactory. Axial and radial profiles of radiative intensity have also been compared with measurements from a radiometer. Disagreements in soot volume fraction and radiative intensity mainly originate from the discrepancies in soot production modeling, which nonetheless can be considered as the state-of-the art. Achieving a better soot prediction is definitely one of the key steps to improve the overall quality of radiation modeling for highly sooting flames but the presented analyses and conclusions can be considered as general. The qualitative physics will be only marginaly affected by the use of more accurate models that will be developed in the future.

Among the total radiative heat transfer from the flame, soot particles are responsible for 21% of the total volume integrated radiative power. However, in regions of high soot volume fraction (≈ 1 ppm), the major contribution to the radiative power largely comes from soot particles. Discrepancies between radiative intensity predictions and experiments are mainly found in these regions and are therefore linked to discrepancies observed in soot volume fraction predictions.

Numerical results are then considered for a detailed analysis of the predicted thermal radiation in the studied case. The impact of reabsorption phenomenon is first investigated. Strong reabsorption is observed with approximatively half of the emitted radiative power being reabsorbed. Depending on their respective transmissivities and therefore their optical thicknesses, different gas bands contribute on a different manner to the total absorbed radiative power. For several of them, which are the main contributions, an optically thin medium assumption is not valid and reabsorption must be considered. Regarding soot particles, the optical thickness is moderate or large at high wavenumbers for regions with high values of soot volume fraction. Finally, for the investigated flame, radiative interactions between gas and solid phases are negligible due to the small overlapping of their absorption coefficient spectrum.

Turbulence radiation interactions (TRI) effects on mean emitted, absorbed and total radiative powers have then been studied. Such effects account for approximatively 12-14% of the spatial integration of these fields. However, the detailed analysis unreavel a more complex story. First, local magnitudes of TRI effects can be much larger, in particular in the presence of soot. Secondly, the TRI effects on gaseous and soot contributions to the mean emitted power are in fact significant but have opposite signs. This partially cancels the magnitude of the total net TRI effects in the studied flame.

A closure model for TRI effects on the mean emitted radiative power has finally been proposed. Very good agreement is achieved when comparing to coupled LES results. The soot contribution is dominated by a negative cross-correlation term between soot volume fraction and temperature. The intermittent nature of soot formation induces large fluctuations in the soot volume fraction, which then enhances this TRI contribution. An interesting impact of soot dynamics on temperature fluctuations through thermal radiation was also revealed. The anti-correlation nature between soot volume fraction and temperature and its consequences will deserve further studies.

A wide range of complex phenomena is captured by the retained modelling setup based on coupled Monte-Carlo large-eddy simulation. Investigation of other jet flames and other configurations will allow generalization of the present conclusions. Nevertheless, several uncertainties remain in the present simulation such as in the formation of soot particles for example. The subfilter-scale TRI effects, in particular due to the soot subgrid-scale intermittency, will also have to be further investigated. Interestingly, the closure model for TRI effects on emitted radiative power derived in Sec. 4.3 can be directly transposed for subfilter-scale modeling. Another limitation dwells in the description of soot particles radiative properties. In recent studies, the morphology of soot fractal aggregates has been shown to drastically increase soot particles absorption coefficient [47, 48] compared with those predicted with the Rayleigh's theory for spherical particles. Future work should be conducted to assess and correct these limitations in order to better describe radiative transfer in sooting flames.

Acknowledgments

This study is supported by the Air Liquide, CentraleSupelec and CNRS Chair on oxycombustion and heat transfer for energy and environment and by the OXYTEC project, grant ANR-12-CHIN-0001 of the French Agence Nationale de la Recherche. Part of this work was performed using HPC resources from the *Mésocentre* computing center of CentraleSupélec and École Normale

Supérieure Paris-Saclay supported by CNRS and Région Île-de-France. The study was also granted access to the HPC resources of CINES under the allocations 2016-020164 and 2017-A0022B10159 made by GENCI.

References

[1] P. J. Coelho, Detailed numerical simulation of radiative transfer in a nonluminous turbulent jet diffusion flame, Combust. Flame 136 (4), (2004) 481–492.

[2] P. J. Coelho, Numerical simulation of the interaction between turbulence and radiation in reactive flows, Prog. Energy Combust. Sci. 33 (4), (2007) 311–383.

[3] A. Wang, M. F. Modest, D. C. Haworth, L. Wang, Monte Carlo simulation of radiative heat transfer and turbulence interactions in methane/air jet flames, J. Quant. Spectrosc. Radiat. Transf. 109 (2), (2008) 269–279.

[4] T. Ren, M. F. Modest, D. C. Haworth, Simulating turbulence–radiation interactions using a presumed probability density function method, Int. J. Heat Mass Transfer 121, (2018) 911–923.

[5] D. Poitou, J. Amaya, M. El Hafi, B. Cuénot, Analysis of the interaction between turbulent combustion and thermal radiation using unsteady coupled LES/DOM simulations, Combustion and Flame 159 (4), (2012) 1605–1618.

[6] A. Gupta, D. C. Haworth, M. F. Modest, Turbulence-radiation interactions in large-eddy simulations of luminous and nonluminous nonpremixed flames, Proc. Combust. Inst. 34 (1), (2013) 1281–1288.

[7] C. Koren, R. Vicquelin, O. Gicquel, Multiphysics simulation combining large-eddy simulation, wall heat conduction and radiative energy transfer to predict wall temperature induced by a confined premixed swirling flame, Flow Turbul. Combust. 101 (1), (2018) 77–102.

[8] L. Tessé, F. Dupoirieux, J. Taine, Monte Carlo modeling of radiative transfer in a turbulent sooty flame, Int. J. Heat Mass Transfer 47 (3), (2004) 555–572.

[9] L. Wang, M. F. Modest, D. C. Haworth, S. R. Turns, Modelling nongrey gas-phase and soot radiation in luminous turbulent nonpremixed jet flames, Combust. Theor. Model. 9 (3), (2005) 479–498.

[10] G. Pal, A. Gupta, M. F. Modest, D. C. Haworth, Comparison of accuracy and computational expense of radiation models in simulation of non-premixed turbulent jet flames, Proceedings of the ASME/JSME 2011 8th Thermal Engineering Joint Conference, AJTEC2011-44585, (2011) 1–10.

[11] R. S. Mehta, D. C. Haworth, M. F. Modest, Composition pdf/photon monte carlo modeling of moderately sooting turbulent jet flames, Combust. Flame 157 (5), (2010) 982–994.

[12] J. L. Consalvi, F. Nmira, Transported scalar pdf modeling of oxygen-enriched turbulent jet diffusion flames: Soot production and radiative heat transfer, Fuel 178, (2016) 37–48.

[13] J. L. Consalvi, F. Nmira, Absorption turbulence-radiation interactions in sooting turbulent jet flames, J. Quant. Spectrosc. Radiat. Transf. 201, (2017) 1–9.

[14] G. Lecocq, D. Poitou, I. Hernández, F. Duchaine, E. Riber, B. Cuenot, A methodology for soot prediction including thermal radiation in complex industrial burners, Flow Turbul. Combust. 92 (4), (2014) 947–970.

[15] L. Palluotto, N. Dumont, P. Rodrigues, C. Koren, R. Vicquelin, O. Gicquel, Comparison of Monte Carlo methods efficiency to solve radiative energy transfer in high fidelity unsteady 3d simulations, Proceedings of ASME Turbo Expo 2017: Turbomachinery Technical Conference and Exposition, GT2017-64179, (2017) 1–10.

[16] L. Tessé, F. Dupoirieux, B. Zamuner, J. Taine, Radiative transfer in real gases using reciprocal and forward Monte Carlo methods and a correlated-k approach, Int. J. Heat Mass Transfer 45 (13), (2002) 2797–2814.

[17] P. Rodrigues, B. Franzelli, R. Vicquelin, O. Gicquel, N. Darabiha, Unsteady dynamics of PAH and soot particles in laminar counterflow diffusion flames, Proc. Combust. Inst. 36 (1), (2017) 927 – 934.

[18] P. Rodrigues, B. Franzelli, R. Vicquelin, O. Gicquel, N. Darabiha, Coupling an LES approach and a soot sectional model for the study of sooting turbulent non-premixed flames, Combust. Flame 190, (2018) 477–499.

[19] ISF3, international sooting flame (ISF) workshop website, http://www.adelaide.edu.au/cet/isfworkshop/data-sets/, accessed October 2017.

[20] S. P. Kearney, D. R. Guildenbecher, C. Winters, P. A. Farias, T. W. Grasser, J. C. Hewson, Temperature, oxygen, and soot-volume-fraction measurements in a turbulent C_2H_4-fueled jet flame, SANDIA REPORT SAND2015-7968, (2015) 1–28.

[21] C. D. Pierce, P. Moin, Progress-variable approach for large-eddy simulation of non-premixed turbulent combustion, J. Fluid Mech. 504, (2004) 73–97.

[22] M. Ihme, H. Pitsch, Modeling of radiation and nitric oxide formation in turbulent nonpremixed flames using a flamelet/progress variable formulation, Phys. Fluids 20 (5), (2008) 1–20.

[23] Y. Wang, A. Raj, S. H. Chung, A PAH growth mechanism and synergistic effect on PAH formation in counterflow diffusion flames, Combust. Flame 160 (9), (2013) 1667 – 1676.

[24] M. E. Mueller, H. Pitsch, LES model for sooting turbulent nonpremixed flames, Combust. Flame 159 (6), (2012) 2166–2180.

[25] M. E. Mueller, H. Pitsch, Large eddy simulation subfilter modeling of soot-turbulence interactions, Phys. Fluids 23 (11), (2011) 1–20.

[26] P. Rivière, A. Soufiani, Updated band model parameters for H_2O, CO_2, CH_4 and co radiation at high temperature, Int. J. Heat Mass Transfer 55 (13–14), (2012) 3349–3358.

[27] R. Goody, Y. Yung, Atmospheric Radiation: Theoretical Basis, Oxford University Press, (1995).

[28] L. S. Rothman, I. E. Gordon, R. J. Barber, H. Dothe, R. R. Gamache, A. Goldman, V. I. Perevalov, S. A. Tashkun, J. Tennyson, HITEMP, the high-temperature molecular spectroscopic database, J. Quant. Spectrosc. Radiat. Transf. 111 (15), (2010) 2139–2150.

[29] S. A. Tashkun, V. I. Perevalov, CDSD-4000: High-resolution, high-temperature carbon dioxide spectroscopic databank, J. Quant. Spectrosc. Radiat. Transf. 112 (9), (2011) 1403–1410.

[30] M. F. Modest, Radiative Heat Transfer (Third Edition), Academic Press, Boston, (2013).

[31] K. C. Smyth, C. R. Shaddix, The elusive history of $m = 1.57 - 0.56i$ for the refractive index of soot, Combust. Flame 107 (3), pp. 314 – 320 (1996) 314 – 320.

[32] Y. F. Zhang, O. Gicquel, J. Taine, Optimized emission-based reciprocity Monte Carlo method to speed up computation in complex systems, Int. J. Heat Mass Transfer 55 (25–26), (2012) 8172–8177.

[33] T. Schonfeld, M. Rudgyard, Steady and unsteady flow simulations using the hybrid flow solver AVBP, AIAA Journal 37 (11), (1999) 1378–1385.

[34] O. Colin, M. Rudgyard, Development of high-order taylor–galerkin schemes for LES, J. Comput. Phys. 162 (2), (2000) 338–371.

[35] T. J. Poinsot, S. K. Lele, Boundary conditions for direct simulations of compressible viscous flows, J. Comput. Phys. 101 (1), (1992) 104–129.

[36] R. Vicquelin, B. Fiorina, S. Payet, N. Darabiha, O. Gicquel, Couplingn tabulated chemistry with compressible CFD solvers, Proc. Combust. Inst. 33 (1), (2011) 1481 – 1488.

[37] C. Lemieux, Monte Carlo and Quasi-Monte Carlo Sampling, Springer Series in Statistics, Springer New York, (2009).

[38] S. Joe, F. Y. Kuo, Constructing sobol sequences with better two-dimensional projections, SIAM J. Sci. Comput. 30 (5), (2008) 2635–2654.

[39] S. Buis, A. Piacentini, D. Déclat, PALM: a computational framework for assembling high-performance computing applications, Concurr. Comp-Pract. E. 18 (2), (2006) 231–245.

[40] Y. Xuan, G. Blanquart, Effects of aromatic chemistry-turbulence interactions on soot formation in a turbulent non-premixed flame, Proc. Combust. Inst. 35 (2), (2015) 1911–1919.

[41] R. S. Mehta, M. F. Modest, D. C. Haworth, Radiation characteristics and turbulence–radiation interactions in sooting turbulent jet flames, Combustion Theory and Modelling 14 (1), (2010) 105–124.

[42] H. El-Asrag, T. Lu, C. K. Law, S. Menon, Simulation of soot formation in turbulent premixed flames, Combustion and Flame 150 (1), pp. 108–126 (2007) 108–126.

[43] D. Poitou, J. Amaya, M. El Hafi, B. Cuénot, Analysis of the interaction between turbulent combustion and thermal radiation using unsteady coupled LES/DOM simulations, Combust. Flame 159 (4), (2012) 1605–1618.

[44] P. J. Coelho, Turbulence–radiation interaction: From theory to application in numerical simulations, J. Heat Transfer 134 (3), (2012) 1–13.

[45] J. L. Consalvi, F. Nmira, Effects of soot absorption coefficient–Planck function correlation on radiative heat transfer in oxygen-enriched propane turbulent diffusion flame, J. Quant. Spectrosc. Radiat. Transf. 172, (2016) 50–57.

[46] R. Vicquelin, Y. F. Zhang, O. Gicquel, J. Taine, Effects of radiation in turbulent channel flow: analysis of coupled direct numerical simulations, Journal of Fluid Mechanics 753, pp. 360–401 (2014) 360–401.

[47] J. Yon, A. Bescond, F. Liu, On the radiative properties of soot aggregates part 1: Necking and overlapping, J. Quant. Spectrosc. Radiat. Transf. 162, (2015) 197–206.

[48] G. Okyay, Impact of the morphology of soot aggregates on their radiative properties and the subsequent radiative heat transfer through sooty gaseous mixtures, Phd thesis, Université Paris-Saclay, (2016).

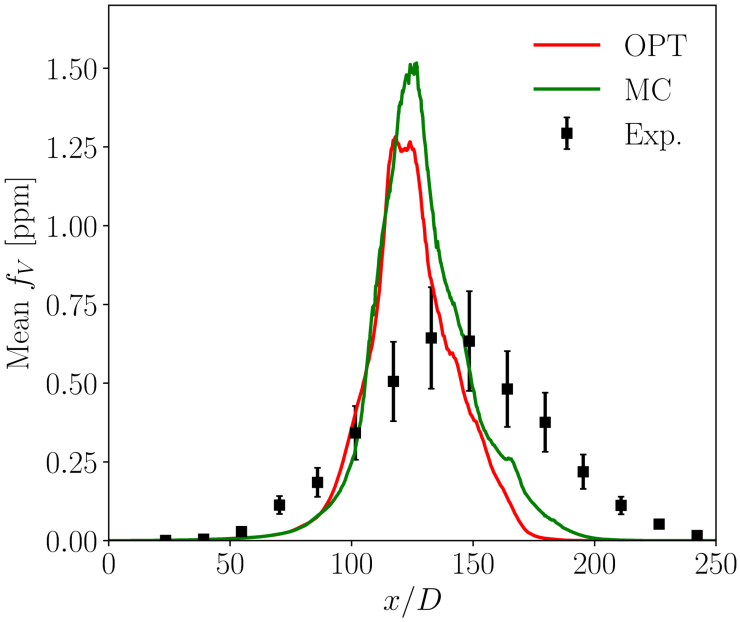

(a) Soot volume fraction axial profile

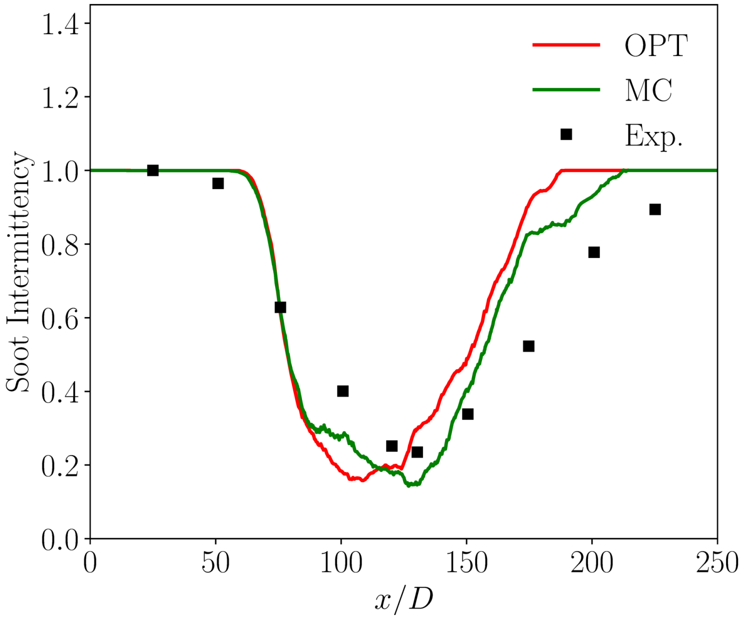

(b) Soot intermittency axial profile

Figure 6. Impact of radiation modeling on soot volume fraction predictions. OPT [18] and MC are respectively represented in red and green solid lines. Experimental measurements from [19] are presented in black squares.

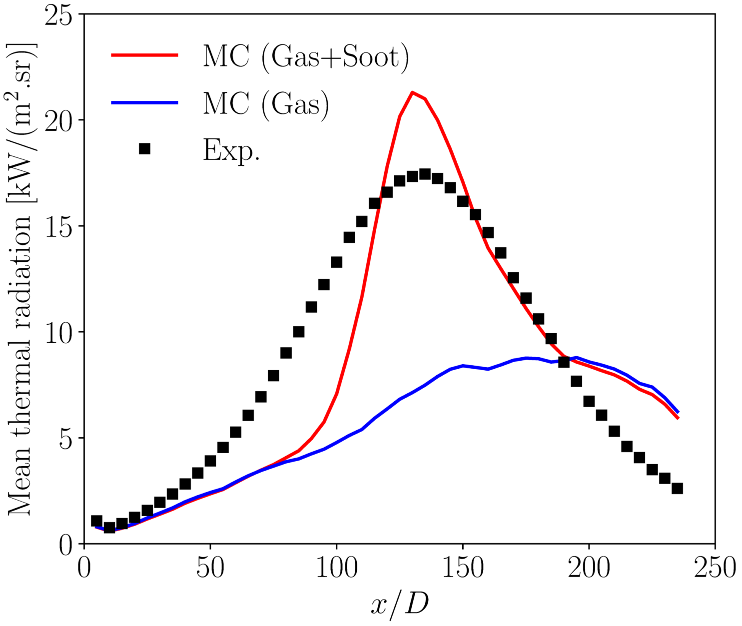

(a) Axial profile

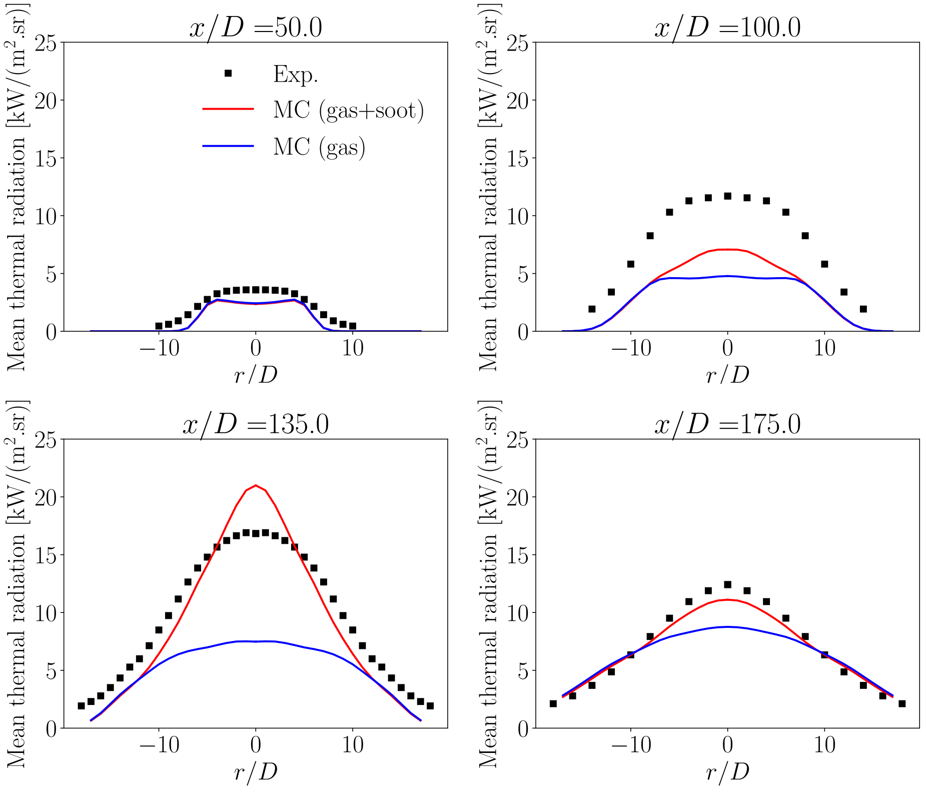

(b) Radial profiles

Figure 7. Comparisons between experimental radiative intensity profiles from [19] and numerical predictions. The contribution of only gaseous phase is plotted in blue, whereas the total contribution is plotted in red.

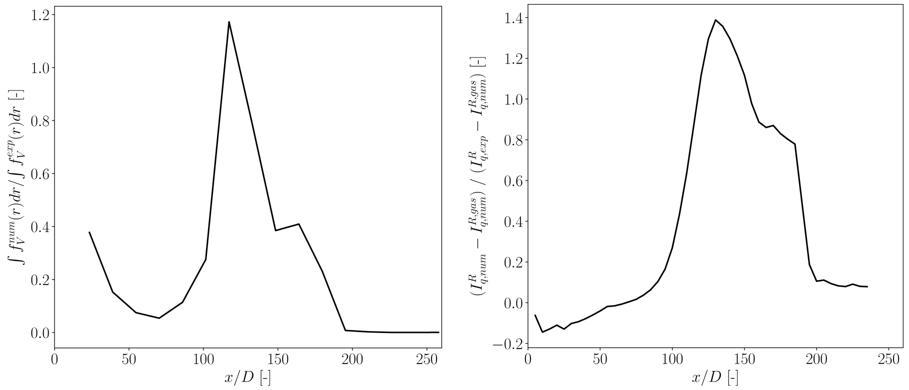

(a) Soot thickness

(b) Soot contribution to radiative intensity

Figure 8. Comparison of soot thickness (left) and estimated soot contribution to radiative intensity (right) between simulations results and experiments.

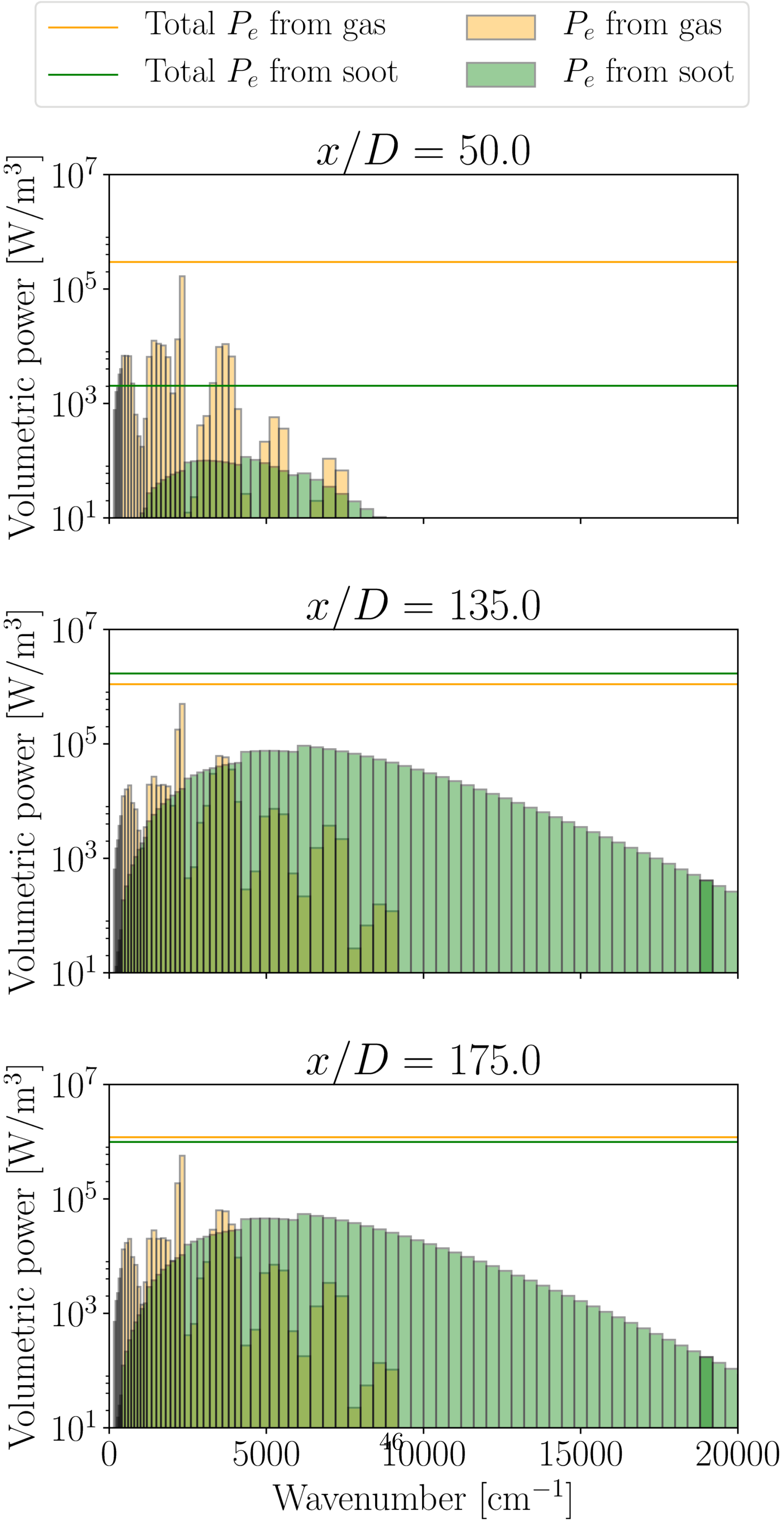

Figure 9. Comparisons of spectral emitted volumetric power from gas (in orange) and soot (in green) at different points. Total emitted power over all the spectrum is represented in orange solid line for gas and in green solid line for soot.

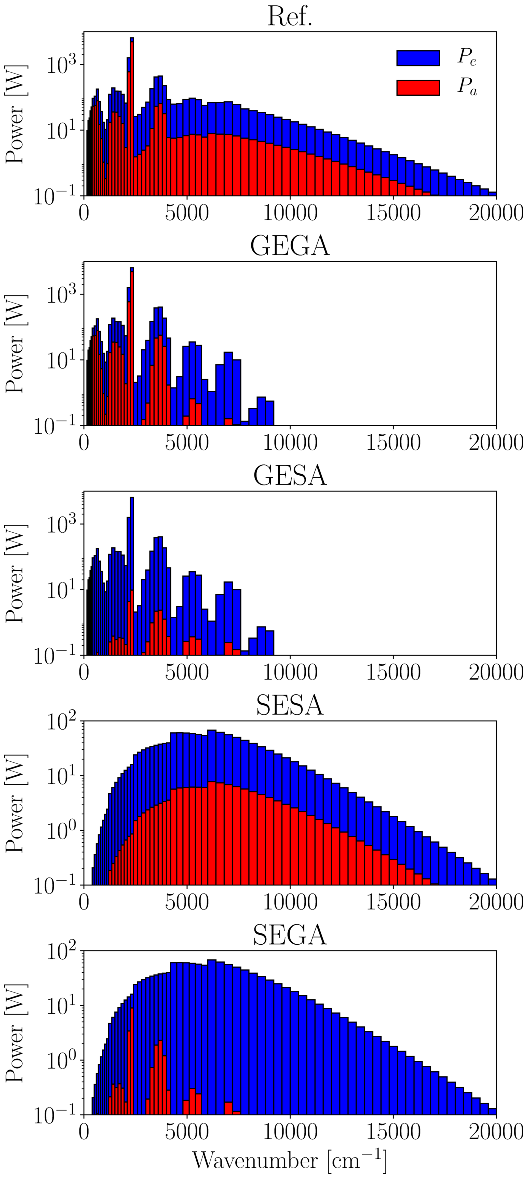

Figure 10. Spectral emitted (blue) and absorbed (red) volume-integrated powers for the instantaneous representative solution. Results with the reference case taking into account gas and soot particles emission and absorption and the four other studied cases: GEGA, GESA, SEGA and SESA.

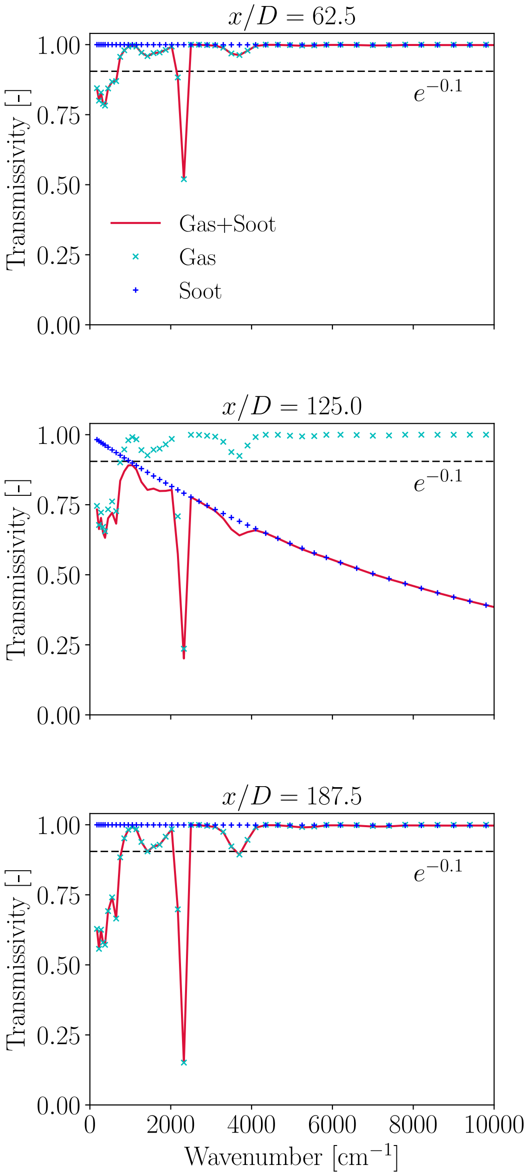

Figure 11. Transmitivity across the flame for different heights above the jet exit. Gaseous and soot contributions are also represented.

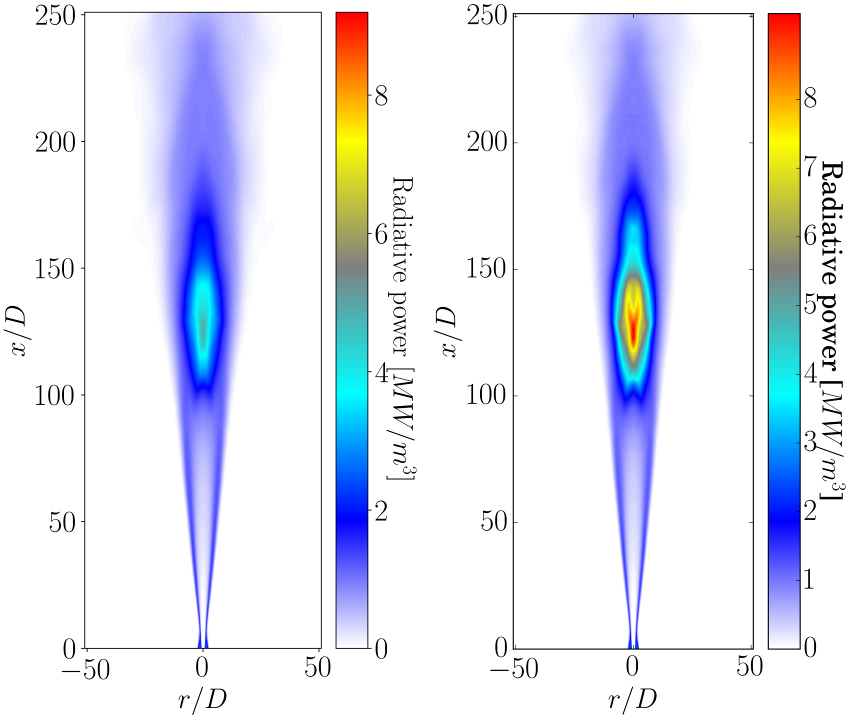

(a) Mean radiative power (b) Radiative power based on mean fields

Figure 12. Comparison between mean field of radiative power issued from the coupled simulation (left) and the one obtained from the resolution of the RTE based on mean fields of temperature, pressure, CO_2 and H_2O molar fractions and soot volume fraction (right).

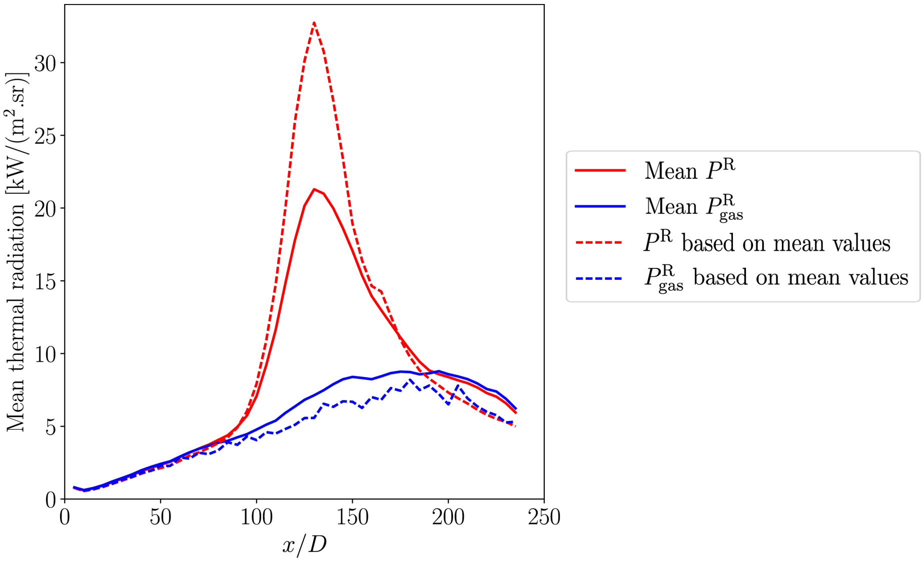

Figure 13. Comparison between radiative intensity profiles obtained with coupled simulation accounting for gas phase (solid blue line) and both gas and solid phases (solid red line) and those obtained solving the radiative transfer equation based on the mean fields of pressure, temperature, CO_2 and H_2O molar fractions and soot volume fraction accounting for gas phase (dashed blue line) and both gas and solid phases (dashed red line).

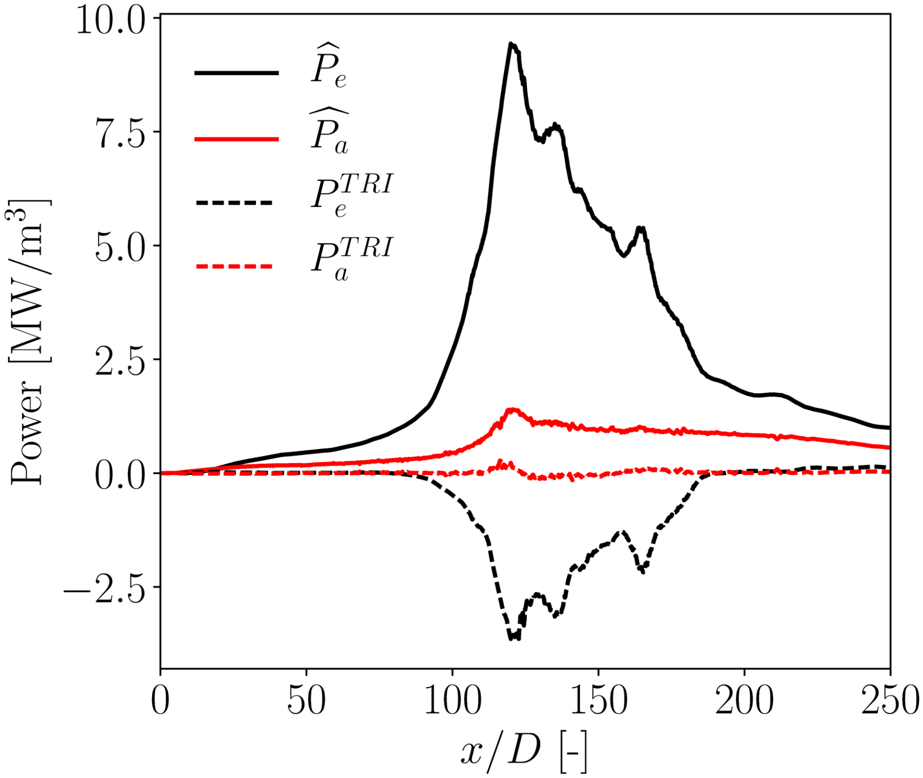

Figure 14. Axial profiles of $\widehat{P_e}$, $\widehat{P_a}$, P_e^{TRI} and P_a^{TRI}.

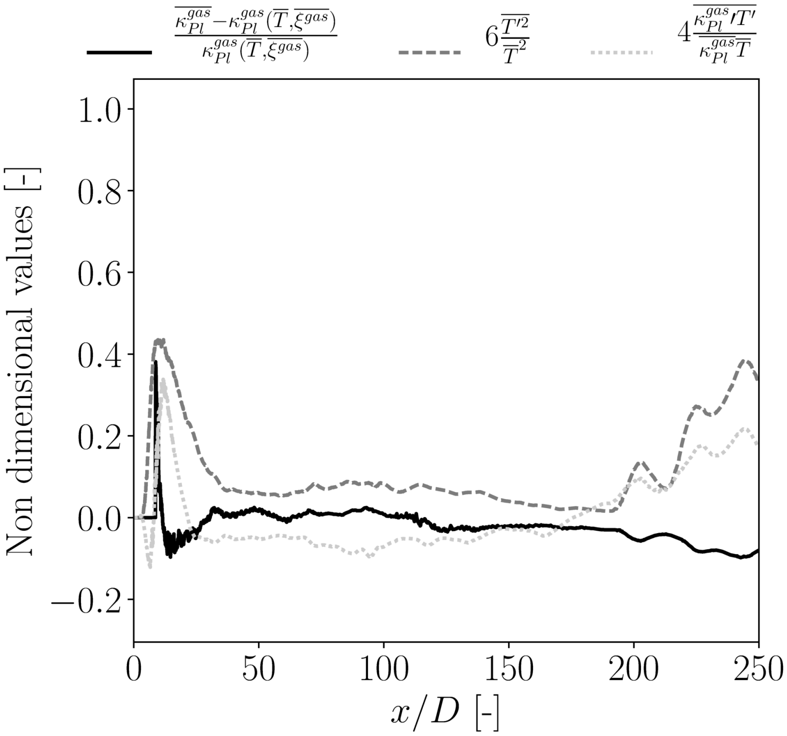

Figure 15. Comparison of TRI terms in the closure model proposed in Eq. (19) for mean gas emitted power.

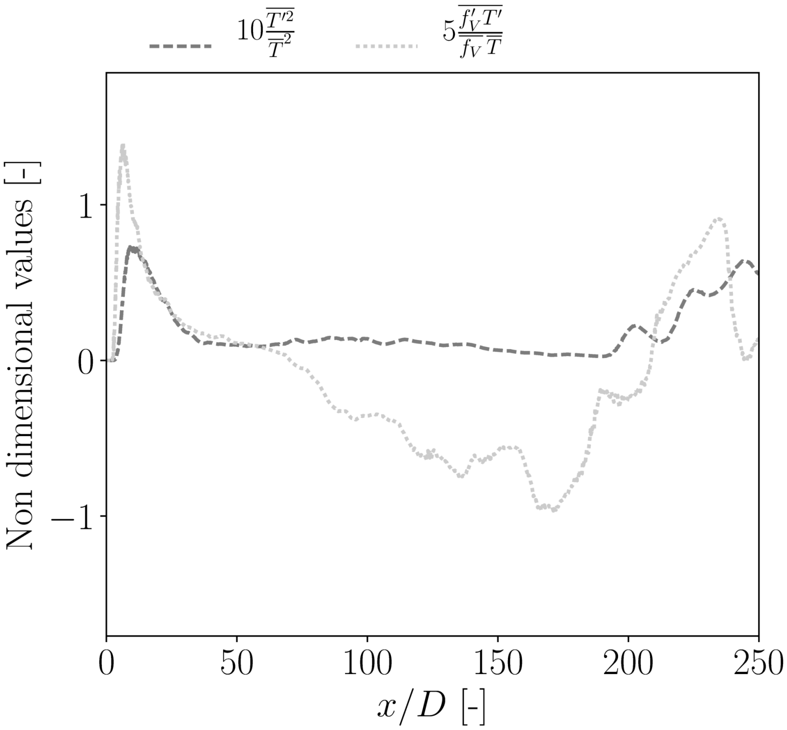

Figure 16. Comparison of TRI terms in the closure model proposed in Eq. (19) for mean soot emitted power.

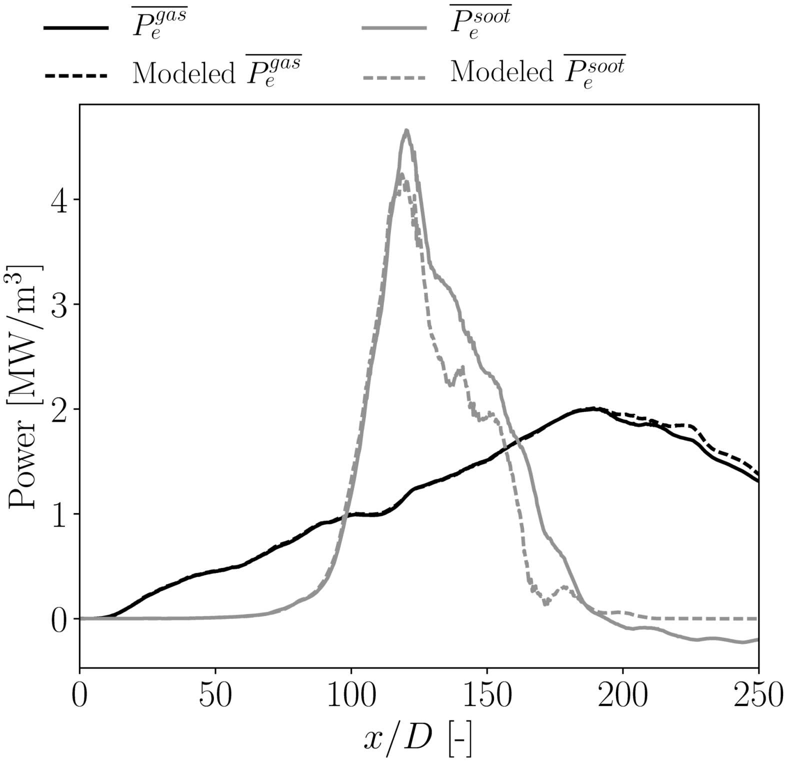

Figure 17. Comparison between axial profiles of exact (from coupled LES) and modeled mean emitted powers from gas and soot phases.

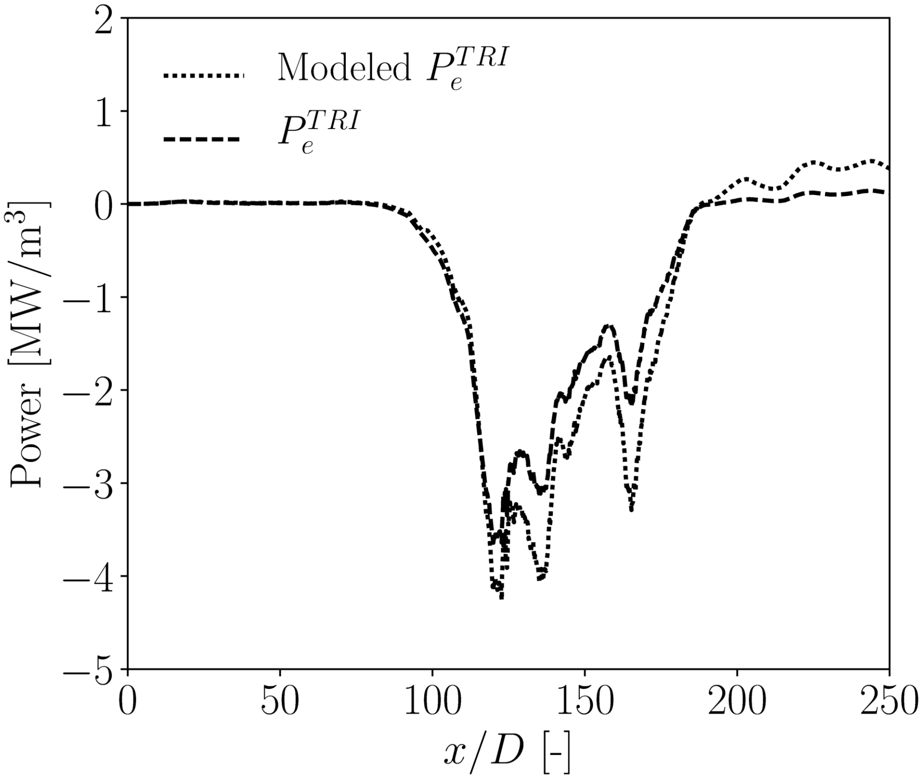

Figure 18. Comparison between exact (from coupled LES) and modeled axial profiles of emitted power TRI contribution.

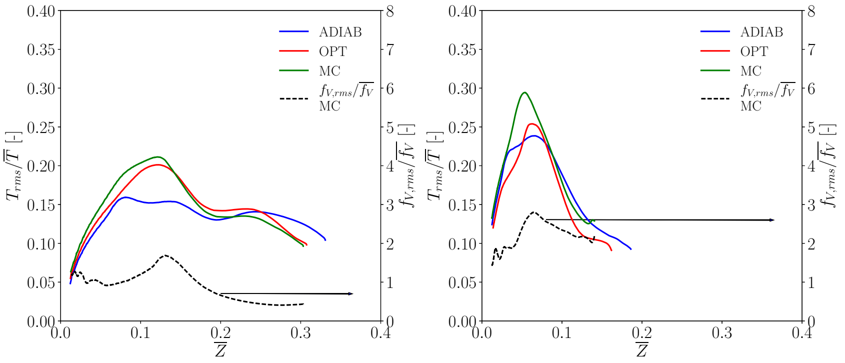

(a) $x/D = 50$

(b) $x/D = 100$

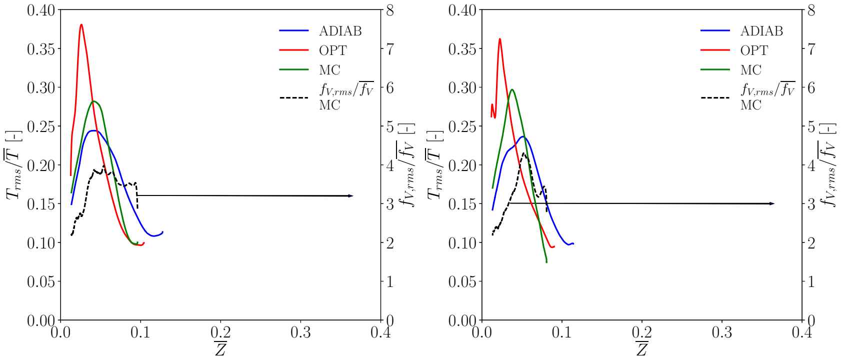

(c) $x/D = 134$

(d) $x/D = 150$

Figure 19. Radial profiles in mean-mixture-fraction space of temperature fluctuation intensity in the three different simulations: adiabatic (ADIAB), optically thin approximation of radiation (OPT) and coupled with Monte Carlo (MC). Profiles are shown for heights $x/D = 50$ (a), $x/D = 100$ (b), $x/D = 134$ (c) and $x/D = 150$ (d).